

## **Library Declaration and Deposit Agreement**

### **1. STUDENT DETAILS**

Tishtrya Ava Mehta  
1763383

### **2. THESIS DEPOSIT**

- 2.1. I understand that under my registration at the University, I am required to deposit my thesis with the University in BOTH hard copy and in digital format. The digital version should normally be saved as a single pdf file.
- 2.2. The hard copy will be housed in the University Library. The digital version will be deposited in the University's Institutional Repository (WRAP). Unless otherwise indicated (see 2.3 below) this will be made openly accessible on the Internet and will be supplied to the British Library to be made available online via its Electronic Theses Online Service (EThOS) service.[At present, theses submitted for a Masters degree by Research (MA, MSc, LLM, MS or MMedSci) are not being deposited in WRAP and not being made available via EThOS. This may change in future.]
- 2.3. In exceptional circumstances, the Chair of the Board of Graduate Studies may grant permission for an embargo to be placed on public access to the hard copy thesis for a limited period. It is also possible to apply separately for an embargo on the digital version. (Further information is available in the Guide to Examinations for Higher Degrees by Research.)
- 2.4. (a) Hard Copy I hereby deposit a hard copy of my thesis in the University Library to be made publicly available to readers immediately.  
I agree that my thesis may be photocopied.
- (b) Digital Copy I hereby deposit a digital copy of my thesis to be held in WRAP and made available via EThOS.  
My thesis can be made publicly available online.

### **3. GRANTING OF NON-EXCLUSIVE RIGHTS**

Whether I deposit my Work personally or through an assistant or other agent, I agree to the following: Rights granted to the University of Warwick and the British Library and the user of the thesis through this agreement are non-exclusive. I retain all rights in the thesis in its present version or future versions. I agree that the institutional repository administrators and the British Library or their agents may, without changing content, digitise and migrate the thesis to any medium or format for the purpose of future preservation and accessibility.

## **4. DECLARATIONS**

### **4.1. I DECLARE THAT:**

- I am the author and owner of the copyright in the thesis and/or I have the authority of the authors and owners of the copyright in the thesis to make this agreement. Reproduction of any part of this thesis for teaching or in academic or other forms of publication is subject to the normal limitations on the use of copyrighted materials and to the proper and full acknowledgement of its source.
- The digital version of the thesis I am supplying is the same version as the final, hardbound copy submitted in completion of my degree, once any minor corrections have been completed.
- I have exercised reasonable care to ensure that the thesis is original, and does not to the best of my knowledge break any UK law or other Intellectual Property Right, or contain any confidential material.
- I understand that, through the medium of the Internet, files will be available to automated agents, and may be searched and copied by, for example, text mining and plagiarism detection software.

### **4.2. IF I HAVE AGREED (in Section 2 above) TO MAKE MY THESIS PUBLICLY AVAILABLE DIGITALLY, I ALSO DECLARE THAT:**

- I grant the University of Warwick and the British Library a licence to make available on the Internet the thesis in digitised format through the Institutional Repository and through the British Library via the EThOS service.
- If my thesis does include any substantial subsidiary material owned by third-party copyright holders, I have sought and obtained permission to include it in any version of my thesis available in digital format and that this permission encompasses the rights that I have granted to the University of Warwick and to the British Library.

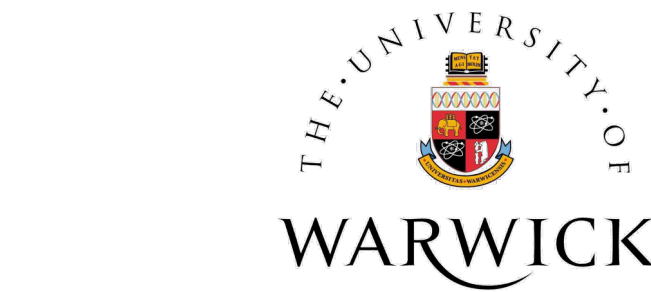
## **5. LEGAL INFRINGEMENTS**

I understand that neither the University of Warwick nor the British Library have any obligation to take legal action on behalf of myself, or other rights holders, in the event of infringement of intellectual property rights, breach of contract or of any other right, in the thesis.

---

*Please sign this agreement and return it to the Graduate School Office when you submit your thesis.*

Student's signature: ..... Date: .....



**Investigating the behaviour of  
quasi-periodic pulsations in solar flares using  
Empirical Mode Decomposition**

by

**Tishtrya Ava Mehta**

**Thesis**

Submitted to The University of Warwick

for the degree of

**Master of Science**

**Department of Physics**

September 2018

THE UNIVERSITY OF  
**WARWICK**

# Contents

<b>List of Tables</b>	iii
<b>List of Figures</b>	iv
<b>Acknowledgments</b>	vi
<b>Declarations</b>	vii
<b>Abstract</b>	ix
<b>Abbreviations</b>	x
<b>Chapter 1 Introduction</b>	1
1.1 The solar structure . . . . .	1
1.2 Sunspots and solar flares . . . . .	4
1.2.1 Impact on space weather . . . . .	6
1.3 Quasi-periodic pulsations . . . . .	7
1.3.1 Physical mechanisms responsible for QPPs . . . . .	8
1.4 Thesis outline . . . . .	11
<b>Chapter 2 Signal Analysis and Instrumentation</b>	12
2.1 Instruments . . . . .	12
2.1.1 Nobeyama Radioheliograph . . . . .	12
2.1.2 GOES . . . . .	13
2.1.3 <i>Fermi</i> . . . . .	14
2.1.4 RHESSI . . . . .	15
2.1.5 <i>Vernov</i> . . . . .	15
2.2 Data analysis techniques . . . . .	16
2.2.1 Fourier analysis . . . . .	16

2.2.2	Wavelet analysis . . . . .	17
2.2.3	Empirical Mode Decomposition . . . . .	18
2.2.4	Interpreting an EMD spectrum . . . . .	23
<b>Chapter 3</b>	<b>Hare and Hounds exercise</b>	<b>28</b>
3.1	Introduction . . . . .	28
3.2	Creating the flares . . . . .	28
3.3	Detection methods . . . . .	29
3.4	Summary . . . . .	31
<b>Chapter 4</b>	<b>Investigating hard X-ray sources at flaring loop footpoints</b>	<b>35</b>
4.1	Introduction . . . . .	35
4.2	Data analysis . . . . .	36
4.3	Errors arising due to precession and nutation in the RHESSI spacecraft .	36
4.4	Summary . . . . .	38
<b>Chapter 5</b>	<b>Quasi-periodic pulsations observed in a single active region</b>	<b>39</b>
5.1	A comparison of analysis techniques . . . . .	40
5.1.1	Data analysis via generation of a periodogram . . . . .	40
5.1.2	Results and discussion . . . . .	40
5.2	Scaling of QPP properties . . . . .	43
5.2.1	Motivation . . . . .	43
5.2.2	Effective quality factors of QPPs . . . . .	44
5.3	Proportionality of amplitude and period in QPPs . . . . .	44
<b>Chapter 6</b>	<b>Discussion and conclusion</b>	<b>50</b>
6.1	Discussion of findings . . . . .	50
6.1.1	Remarks on the use of EMD in the context of solar data . . . . .	50
6.1.2	Mechanisms needed for the classification of QPPs . . . . .	51
6.1.3	Further work . . . . .	52
<b>Appendix A</b>	<b>Comparison of results from Chapter 5</b>	<b>57</b>

# List of Tables

1.1	GOES flare classification . . . . .	5
2.1	Comparison between Fourier, wavelet and EMD analysis . . . . .	19
3.1	Methods employed during Hare and Hounds Exercise 1 . . . . .	30
A.1	Results from analysis in Chapter 5 from Nobeyama RadioHeliograph . . .	58
A.2	Results from analysis in Chapter 5 from <i>Vernov</i> . . . . .	58
A.3	Results from analysis in Chapter 5 from <i>Fermi</i> . . . . .	58
A.4	Results from analysis in Chapter 5 from GOES . . . . .	59

# List of Figures

1.1	A sunspot as imaged by the Solar Optical Telescope (SOT) aboard <i>Hinode</i>	2
1.2	Images of the chromosphere and a coronal loop	3
1.3	Lightcurves exhibiting quasi-periodic behaviour, as observed by Nobeyama and <i>Yohkoh</i>	7
1.4	A sketch illustrating how quasi-periodic behaviour may be driven by an external driver	8
2.1	Lightcurve obtained by GOES showing the profile of a flare in different wavebands	14
2.2	A visualisation of how FFT decomposes a signal in the frequency domain	17
2.3	A synthetic signal seen in the time domain and expressed in a Fourier power spectrum and an EMD spectrum	25
2.4	Analysis of a synthetic signal with prescribed white and coloured noise	26
2.5	Analysis of a synthetic signal with white and non-prescribed coloured noise	27
3.1	Analysis of a flare presented in Hare and Hounds Exercise 1	32
3.2	Comparison of accuracy for three method's output periods in Hare and Hounds Exercise 1	33
3.3	Comparison of statistically significant IMFs from EMD analysis of four non-stationary signals presented in Hare and Hounds Exercise 1	34
4.1	Illustration of an asymmetric eruption of a MFR beneath an arcade	36
4.2	Analysis of a lightcurve obtained from RHESSI	37
4.3	Evidence of underlying oscillation in RHESSI data	38
5.1	Comparison of output periods from Methods 1 and 2	41
5.2	Analysis of a lightcurve exhibiting non-stationary behaviour	42
5.3	Analysis of a lightcurve using a periodogram based approach	43

5.4	Histogram of the number of oscillation cycles observed and distribution of their mean periods . . . . .	45
5.5	Analysis of a lightcurve exhibiting non-stationary behaviour to extract a quality factor . . . . .	47
5.6	Analysis of a lightcurve exhibiting non-stationary behaviour to look for scaling between instantaneous period and amplitude . . . . .	48
5.7	Evidence of scaling of instantaneous period and amplitude . . . . .	49

# Acknowledgments

I would like to extend my sincere thanks to the many members from the Centre for Fusion, Space and Astrophysics here at the University of Warwick for their kind support throughout this degree, in particular to my supervisor Prof. Valery Nakariakov who has been incredibly helpful and given me wonderful guidance during the last year. Additionally I would like to thank Dr. Chloë Pugh for her patience and valuable insight in answering my endless questions and emails, and to Dr. Dmitrii Kolotkov for his continued encouragement and some superb cups of tea!

To my wonderful friends, Katarina Blow, Selina-Jane Spencer, and Mr. Quackers — thank you for always being there to help me debug my code, the many hot drinks, and for all the laughs we shared.



“Finger guns”— *T. Mehta et al. (2018)*

# Declarations

I am submitting this thesis to the University of Warwick as a candidate for the degree of Masters of Science (by Research). The following work has not been submitted as part of any previous degrees and has been carried out by the author, aside from the below cases:

The data used for comparison in Chapter 5 has been provided and collated by C. E. Pugh. In addition, the data from *Vernov*/DRGE which was used in Chapter 5 was prepared by A. V. Bogomolov and I. N. Myagkova. Data from the flaring events discussed in Chapter 4 was collected using RHESSI and collated by I. Zimovets. The raw data, as well as the trends of the lightcurves used in Section 5.2, was collected and determined by D. Kolotkov.

The code performing Empirical Mode Decomposition that is used throughout the thesis was initially developed by S. Anfinogentov, D. Kolotkov, C. E. Pugh and modified by the author.

The work presented in this thesis has been used in the following peer-reviewed articles, of which 1 is in press and 1 is in prep.

- “Non-stationary quasi-periodic pulsations in solar and stellar flares” by Nakariakov, V. M., Kolotkov, D., Kupriyanova, E., Mehta, T., Pugh, C. E., Lee, D.-H., Broomhall, A.-M. (2018) *Plasma Physics and Controlled Fusion*, (in press)
- “Quasi-periodic pulsations of solar and stellar flares: A Hare and Hounds exercise to test the robustness of detections” by Broomhall, A.-M., Hayes, L., Inglis, A., Kolotkov, D., McLaughlin, J., Mehta, T., Nakariakov, V. M., Notsu, Y.,

Pugh, C. E., Van Doorsselaere, T. (2018) *Astrophysical Journal*, (in prep.)

The research discussed in this thesis was also presented at three international workshops:

- “Russian-UK workshop; Seismology of Solar Coronal Active Regions”, Russian Space Research Institute (IKI), Russia, (February, 2018)
- “Quasi-Periodic Pulsations in Stellar Flares: a Tool for Studying the Solar-Stellar Connection”, International Space Science Institute (ISSI), Switzerland, (February, 2018)
- “International ERC AdG Workshop; Magnetohydrodynamic Seismology of the Solar Corona”, Centre for Fusion, Space and Astrophysics; University of Warwick (CFSUA), U.K., (March, 2018)

# Abstract

This thesis concerns itself with the technique of the Empirical Mode Decomposition (EMD) in the context of solar data. This thesis examines the accuracy and applicability of this method against other spectral analysis techniques. In particular EMD is suited to dealing with non-stationary properties of oscillatory signals which are very often observed in quasi-periodic pulsations (QPPs). QPPs are small, roughly periodic variations in intensity often observed during solar and stellar flares. This method is intended to be a complementary or alternative analysis technique to Fourier analysis, which is poorly equipped to handle anharmonic and non-stationary signals. It is of great interest to the solar community to gain a better understanding of the regime(s) generating QPPs as they allow for a deeper understanding of the mechanisms driving solar flaring activity. Successfully isolating said mechanisms could allow for QPPs to be used as diagnostic tools with which to probe the solar atmosphere. As QPPs are a common feature of solar flares, any proposed explanation for flaring behaviour would be incomplete without inclusion of QPP mechanisms and properties. Thus the study of QPPs holds the potential for great impact in the solar physics community, and these phenomena must be examined with appropriate techniques that can handle the many different behaviours observed. Using data obtained from a number of facilities, this thesis puts forward several projects that have been carried out with techniques such as EMD. Data was initially modelled with known parameters to test the accuracy of EMD alongside traditional signal analysis techniques such as Fourier and wavelet analysis. Following this, the technique was used again to look at simulated flaring events blindly in a so-called ‘Hare and Hounds’ exercise. The results of this exercise revealed the greater proficiency of EMD at extracting non-stationary signals against periodogram based methods, at the expense of both computational efficiency and speed. Finally EMD was implemented on solar data from a range of wavebands and instruments, wherein it was compared to previously published results that used a periodogram based methodology [Pugh et al., 2017b]. This resulted in 73% (32 out of 44) of QPP candidates observed by both methods to have the same period ( $\pm 5$  seconds), suggesting that EMD presents reasonably accurate results however is best suited to non-stationary data where the benefits of extracting a well defined anharmonic signal outweigh the difficulties associated with the time-intensive method.

# Abbreviations

AIA	Atmospheric Imaging Assembly.
AR	Active region.
CME	Coronal mass ejection.
DRGE	Detector of the Roentgen and Gamma-ray Emissions.
EVE	Extreme ultraviolet Variability Experiment.
FFT	Fast Fourier Transform.
GBM	Gamma-Ray Burst Monitor.
GOES	Geostationary Operational Environmental Satellite.
HXR	Hard X-ray.
HXT	Hard X-ray Telescope.
ISSI	International Space Science Institute.
LAT	Large Area Telescope.
MFR	Magnetic flux rope.
MPIL	Magnetic polarity inversion line.
NASA	National Aeronautics and Space Administration.
NOAA	National Oceanic and Atmospheric Administration.
NoRH	Nobeyama RadioHeliograph.
QPPs	Quasi-periodic pulsations.
RHESSI	<i>Reuven Ramaty High Energy Solar Spectroscopic Imager.</i>
SDO	Solar Dynamics Observatory.
SXR	Soft X-ray.
XRS	X-ray sensor.

# Chapter 1

## Introduction

### 1.1 The solar structure

The Sun lying close to 147 million kilometres away, at the perihelion of Earth's orbit, emits light across many wavelengths, generated by nuclear fusion occurring in the solar core in a process which requires immense temperatures and pressures. Due to these extreme conditions, the Sun's hydrogen-rich mass forms a plasma, with its density decreasing radially from the core up to a pseudo-surface where the solar atmosphere begins. The solar interior consists of three regions: the core; radiative zone; and convective zone. The core, defined from the centre to around 0.25 solar radii ( $R_\odot$ ), reaches  $15 \times 10^6$  K and contains the region in which fusion from hydrogen to helium and heavier elements is allowed to occur. Moving radially out, the radiative zone extends to roughly  $0.7 R_\odot$  where energy released from the core is transferred primarily by thermal radiation. The dominant method of energy dissipation is overtaken by convection in the convective zone which extends to the solar surface. It should be noted that the term 'solar surface' is misleading, as the Sun has no cut-off point in density or in the phase of matter, where a solid lies beneath a gas. Although the plasma density does decrease rapidly above the radiative zone, it is more sensible to define a surface (from here on in referred to as the photosphere, as the level at which the Sun becomes opaque to visible light) extending radially out from  $1 R_\odot$  for  $\approx 400$  km. In the convection zone, heat flows pull hot solar material toward the surface where it cools by radiation, increases in density, and falls back towards the interior. This cyclic behaviour leads to granulation patterns which can be seen in Figure 1.1, similar to what can be seen on the surface of a pan of boiling water. The rising bubble of plasma is hotter than the cooler sinking boundaries, creating a continuous cycle of emerging and dissipating granulation cells which cover the photosphere.

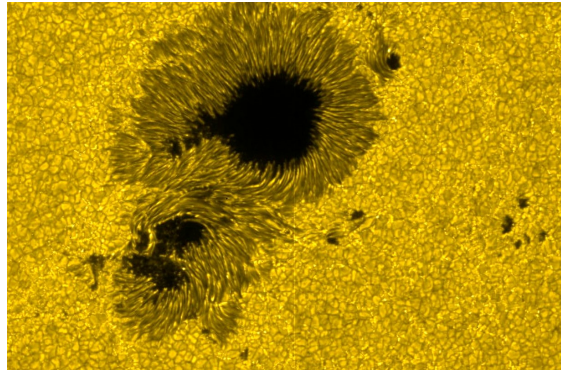
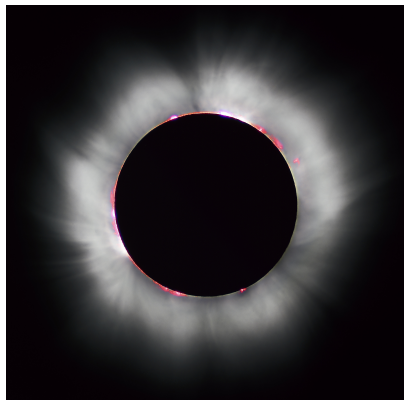


Figure 1.1: A sunspot as seen by the Solar Optical Telescope (SOT) aboard *Hinode* can be seen extending across the centre of the image surrounded by much smaller scale granules (the individual convection cells) present on the entirety of the image as small bubble-like structures. Collectively this behaviour is known as granulation. *Image courtesy of National Aeronautics and Space Administration (NASA)*.

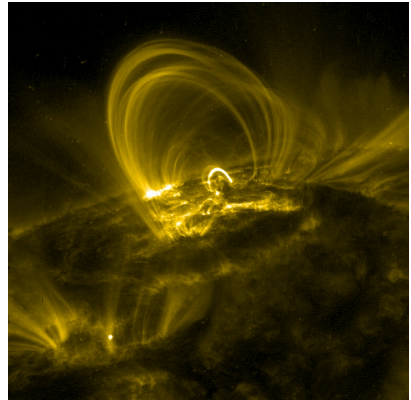
Surface granules typically exist for tens of minutes and are around 1500 km in width [Bahng & Schwarzschild, 1961], and major granulation cells are thought to exist as ‘super granules’ which have typical lifetimes of several hours and extend to approximately 16000 km as established in Leighton et al. [1962].

Extending above the photosphere lies the chromosphere which is best observed in the hydrogen-alpha filter ( $\text{H}\alpha$ ). This filter is used to great effect to view the solar disk and other structures with comparably cool temperatures, such as spicules (jets of cooler plasma which quickly rise up into the corona and rapidly decay). The chromosphere, as seen in Figure 1.2a, is made visible during solar eclipses, when its reddish colouring can briefly be seen amongst the glow of the surrounding corona. The corona is the outermost layer of the solar atmosphere and is structured by both closed and open magnetic field lines in an evolving configuration which is driven by solar rotation and movement of the solar interior led by convection currents. This causes field lines to become highly sheared and twisted, providing ideal conditions for magnetic field line reconfiguration which leads to behaviour such as solar flares and coronal mass ejections (CMEs), as discussed in Section 1.2. The corona is separated from the chromosphere by the transition region in which the plasma density decreases by two orders of magnitude and the temperature increases from 20,000 K to above 1 MK, in what is known as the coronal heating problem; one of the more elusive questions put forward to the solar community today is the driving force for this heating. A popular proposed solution is heating through magnetohydrodynamic (MHD) waves but as of yet no regime has

been confirmed by observational results. A number of structures, such as prominences and coronal loops, are seen in the corona as pictured in Figure 1.2b. Prominences (also known as filaments when viewed on-disk) are categorised as large strands of cool plasma suspended in the corona, guided by surrounding magnetic fields, with one or two footpoints usually found on the photosphere. Prominences can be seen to appear directly above lines of magnetic polarity inversion (a line that separates two regions of strongly opposing magnetic polarity) and typically have lengths on the scale of several thousand kilometres and may exist for weeks or months. Usually this results in a rapid release of energy that takes place over a matter of hours, redefining the structure as an eruptive prominence. Coronal loops are often found with their footpoints anchored in sunspots, rooted in regions of opposite magnetic polarity (see Section 1.2) and are loops of magnetic flux and high plasma density protruding into the corona. Loops have been seen to oscillate transversely, in what has been suggested to be a standing kink mode, when impacted by an external driver such as a fast magnetoacoustic wave emitted from a nearby flare or CME. Recent results show evidence of a second harmonic within these oscillations which has implications for how we understand and interpret the mechanisms that drive and dampen the motion of coronal loops [Duckenfield et al., 2018].



(a) The chromosphere (red) made visible by a solar eclipse.



(b) A coronal loop seen off the limb of the Sun in 171Å

Figure 1.2: Left: This solar eclipse was photographed on August 11<sup>th</sup> 1999 and shows parts of the chromosphere as a discontinuous red band of light which has become visible as the Moon obscures the disk of the Sun. The corona can be seen as a white region surrounding the Sun and can be seen to extend deep into the surrounding space, without an official upper limit. *Image courtesy of L. Viatour.* Right: An image taken by the Transition Region and Coronal Explorer (TRACE) showing a hot coronal loop extending out from an active region. *Image courtesy of NASA.*

## 1.2 Sunspots and solar flares

A sudden release of free magnetic energy in a localised region (usually above a sunspot) is characterised as a solar flare, and can appear in a wide range and combination of energy bands, from radio waves to gamma radiation. This energy originates from magnetic potential energy held in field lines, that can create regions of intense magnetic activity often following a flux tube (a ‘cable’ of magnetic field lines) erupting to the solar surface. These field lines become tangled by surface motions triggering a reconfiguration of the magnetic field. As magnetic fields suppress convection, the most efficient mechanism by which heat is transported to the upper layers of the Sun, the temperature in the photosphere is significantly lower in regions where there is a great amount of magnetic flux. As these regions of high magnetic activity are significantly cooler than the ambient Sun surroundings, dark patches in white light observations can be seen on the photosphere. Therefore sunspots can be used as signage for areas of magnetic activity and can be good indicators as to where the next solar event, such as a solar flare or a CME may occur. The Sun follows a roughly 22 year long solar cycle in which every 11 years the solar activity increases from a minimum to solar maximum and then eases back down. The average magnetic polarity of the North and South poles flips after every 11 years, making the overall cycle periodic over roughly 22 years. Solar maximum is associated with a large number of sunspots seen due to the increase in magnetic activity, which leads to greater numbers of solar flares and CMEs. Conversely during solar minimum, the Sun may be referred to as quiet where limited activity is seen and a lack of sunspots may persist for several weeks. Rudolf Wolf, a Swiss astronomer and mathematician, noticed the Sun’s cyclicity and established a naming system by compiling observations of sunspots from the preceding century and defining Cycle 1 to have occurred between 1755–1766. Since then, cycles have been labelled chronologically. At the time of submitting this thesis, it is predicted that the current solar cycle, Cycle 24, should be concluding during mid-2018 with Cycle 25 reaching solar maximum around 2025, but further evidence of increasing magnetic activity must be observed before this can be confirmed. In Cycle 23 (beginning in May 1996 and ending in January 2008) there was an unusual lack of solar activity, with a total of 805 days in which no sunspots were observed [Phillips, 2008]. The frequency of solar flares is modulated by the position in the solar cycle, and flares may occur daily during solar maximum, whereas during solar minimum only one flare is observed per week on average. However this does not imply that the most powerful flares are confined to solar maximum. Indeed during the solar minimum of Cycle 24 a powerful flare, denoted as SOL2017-09-06T12:02, was observed reaching an X9.3 GOES

classification. Flares with higher energy sometimes accompany CMEs that have the potential to impact the Earth, as discussed in Section 1.2.1.

Flares can be sorted into one of five classifications, depending on their peak flux in watts per square metre of X-rays within 1–8 angstroms ( $\text{\AA}$ ) by the X-ray sensor (XRS) instrument on board the GOES 15 satellite (see Section 2.2) which is at roughly Earth’s orbital distance, in geostationary orbit over the Pacific Ocean. The classification is as follows:

GOES Class	Peak flux ( $\text{Wm}^{-2}$ )
A	$< 10^{-7}$
B	$10^{-7} - 10^{-6}$
C	$10^{-6} - 10^{-5}$
M	$10^{-5} - 10^{-4}$
X	$> 10^{-4}$

Table 1.1: GOES flare classification

A flare is further categorised by a unit between 1 and 9 which indicates its strength within its class (aside for the X class flares which continues in numbering past 9). A unit increase in the GOES classification corresponds to a factor increase in peak flux, i.e. a B5 class flare emits five times the wattage per square metre that a B1 class flare does. For highly energetic events, such as X or M class flares, the impact on Earth can be significant. X class flares are the most powerful of solar phenomena and can trigger radio blackouts, as well as a number of other consequences, when the charged particles emitted by the flare are transported as part of solar wind and interact with the Earth’s ionosphere. Among the highest classified flares in history is an event that took place on November 4<sup>th</sup> 2003 which was recorded to have a weighted mean X-ray peak of 4.0 mW/m<sup>2</sup>, putting it in the region of an X40 classification [Brodrick et al., 2005]. Less energetic M class flares may cause the Northern and Southern lights to increase in frequency and intensity as emitted charged particles follow the Earth’s magnetic field lines to the North and South poles, where they interact giving off visible light as aurorae. C class flares have few noticeable effects on Earth and B and A class flares are better known as microflares and are often taken to be the background flux behind more powerful solar phenomena.

The so-called ‘standard model of a solar flare’ also known as the ‘CSHKP model’ (Carmichael [1964], Sturrock [1966], Hirayama [1974], Kopp & Pneuman [1976]) attributes the rapid expulsion of magnetic energy emitted during a flare to magnetic reconnection occurring between neighbouring field fluxes. The model suggests that following

reconnection at an ‘X-point’ or null point, charged particles follow the field lines to the footpoints where hard X-ray (HXR) emission is generated. This rapid emission of HXR can be used as a tool for spotting reconnection events.

### 1.2.1 Impact on space weather

The solar wind is a stream of plasma emitted from the Sun’s corona which travels radially outwards. Its velocity is highly dependent on its direction of propagation, with the greatest speeds produced near the poles where open field lines are expected. CMEs and solar flares cause additional charged particles to be accelerated away from the solar disk, temporarily increasing the density, temperature and local speed of the surrounding solar wind. This wind may propagate in the direction prescribed by the flare or CME but becomes disperses as it travels and spreads over a larger area. For usual solar events, the wind is diffuse enough that when it reaches 1 AU (the distance of Earth’s average orbit) the charged particles are largely deflected by the ionosphere, the inner edge of the magnetosphere, surrounding the Earth, allowing the Earth to be shielded from the high speed ionising radiation. However when the magnetic activity on the Sun increases, the solar wind in turn increases in density. If charged particles associated with a high energy eruption are directed towards Earth (or more accurately, where the Earth will be in the several hours or number of days it will take for the wind to travel to 1 AU), the wind may cause a significant reconfiguration of the Earth’s magnetosphere. This interaction may interfere with radio communications and cause blackouts, such as the infamous geomagnetic storm of March 1989 in which Quebec was left without power for several hours due to an X15 class flare that occurred several days before. The effects of space weather can be mitigated by forecasting solar activity which allows for more time to prepare for the consequences. Forecasts can be performed by active region (AR) tracking and classification, which takes into account the size, primary penumbra shape and interior spot compactness of the AR. From these properties, the parameters can be quantified to give an overall likelihood of a flaring event. A number of methods may be used to arrive at this probability, such as Bayesian statistics or artificial neural networks, outputting a statistic such as “There is a 20% chance of an X class flare occurring within the next 24 hours”. For example, the flare prediction system on publicly available website Solar Monitor<sup>1</sup> calculates three separate probabilities of a C, M, or X class flare occurring from a given AR in the next 24 hours based on data obtained by *National Oceanic and Atmospheric Administration (NOAA) Space Weather Prediction Center* data using two

---

<sup>1</sup>[www.solarmonitor.org](http://www.solarmonitor.org)

main methods. The first is the MCSTAT method as described in [Gallagher et al., 2002], which uses point-in-time McIntosh classifications to obtain Poisson flaring probabilities. The other is MCEVOL, which follows the 24 hour evolution of McIntosh classifications, again to calculate Poisson flaring probabilities [McCloskey et al., 2016].

### 1.3 Quasi-periodic pulsations

Lightcurves of flaring energy releases of solar and stellar origin often show periodic oscillations in intensity in what are known as quasi-periodic pulsations (QPPs). Usually QPPs are seen to exist for up to tens of cycles and QPPs in solar flares typically show periodicities of several seconds to a number of minutes [Van Doorsselaere et al., 2016]. Successfully modelling QPPs would offer a far deeper understanding of the mechanisms driving solar and stellar energy releases, as the mechanism by which they are generated is not currently known [McLaughlin et al., 2018]. The implications of finding a mechanism, or being able to categorise QPPs into different generation methods is of great importance to the solar physics community as QPPs could be used as a means to study seismological properties of the QPP site. In soft X-ray (SXR), QPPs are most often observed immediately following the impulsive phase of a solar flare, decaying shortly after.

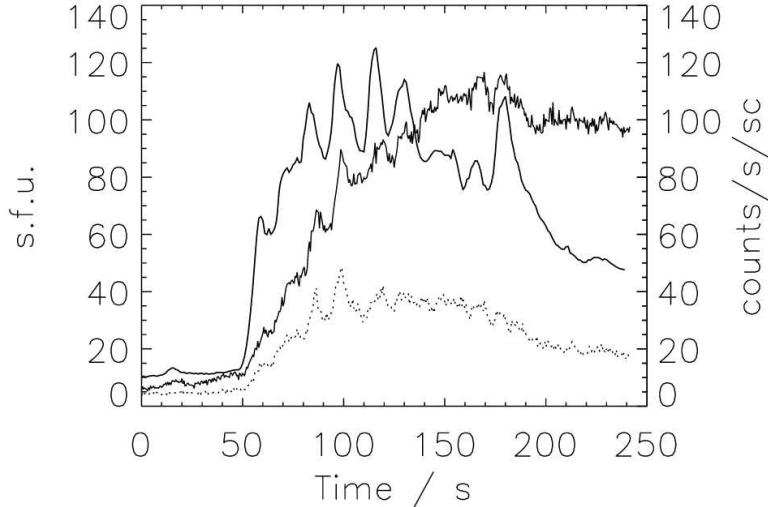


Figure 1.3: This figure shows lightcurves obtained from both Nobeyama Radiohelionograph (in 17 GHz, shown as the thick black line), and *Yohkoh*/ Hard X-ray Telescope (HXT) (thin line for 13–23 keV, dashed for 23–33 keV) for the event SOL1998-05-08T01:57. Some clear quasi-oscillatory behaviour can be seen from 80–200 s. *Figure from [Inglis et al., 2008]*.

### 1.3.1 Physical mechanisms responsible for QPPs

Although QPPs have been reported since 1969 [Parks & Winckler, 1969], seemingly little progress has been made on categorising the methods of production, despite the wealth of observational data and analysis of both temporal and spatial variety. The mechanisms suggested fall into three categories: QPPs driven by an external quasi-periodic modulator inducing magnetic reconnection; mechanisms such as self-driven oscillatory reconnection (where the periodicities are built into the flare itself); or via MHD waves in flaring systems, as further discussed by McLaughlin et al. [2018].

The externally driven QPP mechanism proposes some extrinsic oscillatory driver such as an oscillation in a neighbouring cooler loop, that triggers periodic production of non-thermal particles via a modulated magnetic reconnection rate. The oscillating loop, or other disturbance e.g. another neighbouring flare event, could hit the null point residing above an arcade, inducing periodic reconnection. This was first suggested by Nakariakov et al. [2006] (see Figure 1.4). In particular, this mechanism gives a good explanation for the observation that QPPs are not co-temporal along all wavelengths, as discussed in Dolla et al. [2012]. Although the non-thermal particles would all be generated at the X-point simultaneously, the different propagation speeds and dissipation locations of particles with different energies would naturally lead to the apparent phase shift in QPPs between different wavelength bands.

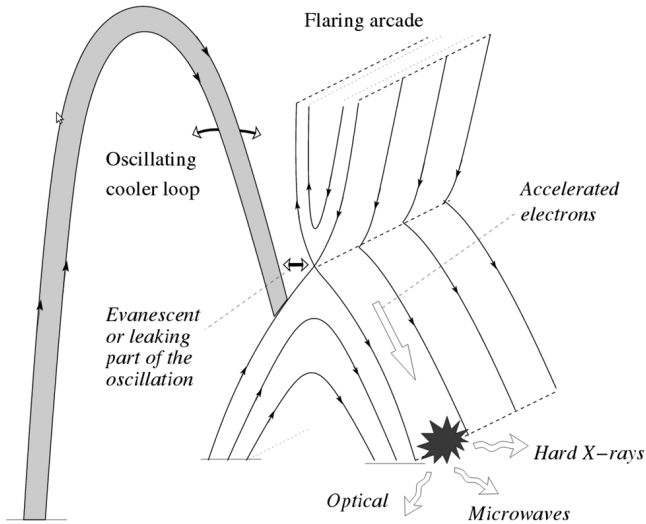


Figure 1.4: A sketch showing how an external driver may modulate the reconnection rate and create QPPs. *Image taken from [Nakariakov et al., 2006].*

Another proposed mechanism for QPPs is a self-driven oscillation wherein the modulation of the reconnection rate is an inherent property of the flare. It is possible that the X-point functions as a resonator for fast waves as described in Craig & McClymont [1991], from which the period of the oscillation is determined by the Alfvén speed profile. The concept of a self-driving oscillation, specifically the ‘magnetic dripping’ model, is further explored in Section 5.2. This mechanism compares the amplitude of an oscillation to the size of droplets falling from a dripping tap. The rate of water leaking out of the tap depends on many properties of the system, including the surface tension of the liquid, the strength of gravity, the rate of inflow into the tap, and so on. As a result relationships between parameters arise; some taps may leak smaller drops of water more frequently than their counterparts which have slower but larger drops. This gives way to an inverse relationship between the volume of water in each drop and its frequency. This mechanism may be compared to regimes where the output of magnetic flux seems to be modulated by its period (or vice versa).

A third candidate for the production of QPPs is MHD waves present or previously excited in the flaring loops. Waves can, of course, transport energy produced in the X-point down to the footpoints and would naturally be reflected at the boundary, setting up standing waves. For example, QPPs in HXR and white light could be explained by the global sausage mode acting on an anchored flaring loop. These QPP emissions are likely produced by bremsstrahlung, a so-called ‘breaking radiation’. Bremsstrahlung is emitted when a charged particle experiences acceleration due to interaction with other charged particles, in this case non-thermal electrons interacting with nuclei as they travel into the denser layers of the solar atmosphere. The flaring loop acts as a magnetic trap keeping non-thermal electrons between the two loop legs, allowing electrons with sufficiently large pitch angles to bounce between them. The critical pitch angle,  $\theta$ , gives the angle at which a particle may strike a footpoint and subsequently be trapped between the two loop legs. The angle is modulated by the ratio of magnetic fields near the top of the loop and at the footpoints, according to

$$\sin^2 \theta = \frac{B_{\text{top}}}{B_{\text{footpoint}}}, \quad (1.1)$$

where  $\theta$  gives the critical pitch angle and  $B_{\text{top}}$  and  $B_{\text{footpoint}}$  give the magnetic field strength at the apex of the loop and at the footpoints respectively. Thus, changes in the strength of the magnetic field towards the top of the flaring loop would change the critical pitch angle for non-thermal particles to be reflected. Therefore, if there were a regime which periodically changed the strength of the magnetic field towards the apex of

the loop, whilst the magnetic field at the footpoints remained constant, this would cause a periodic change in particle flux causing bremsstrahlung radiation. Magnetoacoustic oscillations, and in particular the global sausage mode, are compressive modes. As the sausage mode has a wavelength of twice the loop's length, the apex would be periodically compressed, causing the local particle density to be modulated according to the period of the sausage mode, which in turn would modulate the magnetic field strength. Where the plasma  $\beta$  (the ratio of plasma pressure to magnetic pressure) is sufficiently high this effect can also be associated with the longitudinal mode. This mechanism would allow for multiple modes to be set up, which agrees with the multiple periodicities occasionally seen in QPPs, but does not provide an explanation for the temporal offsets for different energies in QPPs. This proposed regime and others are explored more thoroughly in Nakariakov & Melnikov [2009].

## 1.4 Thesis outline

This thesis covers the behaviour and amuses possible mechanisms for creating QPPs as well as a substantial statistical survey on the use of Empirical Mode Decomposition (EMD) in the context of detecting and studying QPP signals in solar flares. As QPPs are often seen exhibiting anharmonic and non-stationary behaviour there is a need for an adequate analytical tool that does not assume sinusoidal components, such as EMD. Chapter 1 describes the structure of the Sun and introduces the concept of QPPs in a solar context.

In Chapter 2, the instrumentation used to collect solar data is overviewed and the techniques of Fourier and wavelet analyses are discussed. EMD is also introduced as a data analysis technique, and is used upon sample datasets to better equip the reader to correctly interpret the spectra that are seen throughout the thesis.

Chapter 3 introduces the so-called ‘Hare and Hounds’ exercise, in which an International Space Science Institute (ISSI) team<sup>2</sup>, with the author’s participation, was assembled to analyse a number of flares blindly with different analysis techniques, in order to discern which were the most accurate and efficient in extracting the periodicities of simulated QPPs.

In Chapter 4 HXR data from RHESSI was analysed using EMD in order to ascertain if there was any evidence of a hidden periodicity in a noisy signal. The aim of this chapter was to better understand the mechanism that may be at play during the observations of HXR bursts over a short period of time.

Chapter 5 first presents an exploration of the use of EMD against the more traditional periodogram-based approach as outlined in Pugh et al. [2017b]. 53 flares were analysed using EMD and the results were compared with Pugh et al. [2017b] with specific attention drawn to non-stationary cases and the issues that arose in detrending data and taking into account the presence of coloured (or power-law distributed) noise. The chapter then goes on to look at the apparent modulation of instantaneous amplitude with period in a case study of 11 flares in a simple statistical survey. The implications of further study on matters discussed in this chapter may lead to a better understanding of the mechanisms driving (a subset of) QPPs.

Chapter 6 collates the conclusions of the previous chapters and discusses the implications of the findings. Further work and improvements on the methods used in this thesis is suggested. Tables of findings can be found in the attached appendix.

---

<sup>2</sup>[issibern.ch/teams/quasistellflare](http://issibern.ch/teams/quasistellflare)

## Chapter 2

# Signal Analysis and Instrumentation

### 2.1 Instruments

Data from a number of telescopes, both ground and space based, was analysed in this thesis. In particular, the data was required to have a high time cadence to observe QPPs with periods of only a few seconds, and ideally took measurements in channels that could be compared to data from other instruments to confirm the authenticity of signals. Thus the data discussed in this thesis was obtained from the following instruments: Nobeyama RadioHeliograph (NoRH), *Fermi*, Geostationary Operational Environmental Satellite (GOES), *Reuven Ramaty High Energy Solar Spectroscopic Imager* (RHESSI) and *Vernov*. In this chapter we discuss the instrumentation used and introduce EMD as a data analysis technique. EMD is then performed on a number of simple datasets in order to equip the reader with the skills necessary to interpret the results and spectra given throughout the following chapters.

#### 2.1.1 Nobeyama Radioheliograph

NoRH is a ground-based facility in Japan which has been operational since 1992 and was used in this project to observe QPP candidates due to its high temporal resolution; 1 second when steady or 0.1 s during events [Nakajima et al., 1994]. As a radio interferometer, the output is an array of time stamps against correlation values of the telescope's parabolic antennae. These correlation values are analogous to the 2D Fourier components of the solar disk's brightness distribution. NoRH takes measurements in

both the 17 and 34 GHz channels but only data from the 17 GHz channel was used. This is because the 17 GHz channel more proficient at picking up fine structure detail on smaller flares. Thus using the 17 GHz channel gives a better likelihood of seeing well resolved QPPs than in the 34 GHz channel.

### 2.1.2 GOES

Whilst NoRH focuses on the long wavelength solar emission, (seen in the impulsive phase of a flare), the GOES program observes in the far shorter X-ray region. GOES is a joint operation between NASA and NOAA since the launch of the first satellite in 1975, and currently consists of 17 satellites, at least two of which are continually operating in geostationary orbit. This near-continuous view of the solar face allows for a vast wealth of solar flux data to be picked up by the X-ray sensor (XRS) aboard GOES 13–15 which observes across 2 wavebands in the SXR range: 0.5–4 and 1–8 Å.

As seen in Figure 2.1, during a flare intensity peaks in the 0.5–4 Å channel first (blue) and then decays more rapidly than the more gradual rise and decay of intensity as measured in the 1–8 Å channel (red). Measurements in both channels have been used throughout this thesis, as some QPPs are more visible in one channel than the other. This is due to when they occurred during the flare and the signal-to-noise ratio at the given time in that particular channel. The cadence of the XRS aboard GOES is 2.048 s [Machol & Viereck, 2016] which again is sufficiently low to distinguish QPPs of short periods. Despite an excellent signal to noise ratio given by GOES, it would be ideal to suppress the contribution of the trend from the analysis to isolate quasi-periodic signals. This can be done by taking the time derivative of the raw data, as any quasi-periodic signals will be better contrasted to the derivative of a slowly varying background trend. This technique is best employed in the context of SXR measurements, as QPPs observed in this energy range are accompanied by a significant trend showing the sharp rise in intensity of a solar flare. However by taking the time derivative of the data, the output will no longer represent raw SXR data. According to the Neupert effect, which is entirely based on empirical data, the time derivative of SXR gives a close correlation with HXR emission in a solar flare [Veronig et al., 2005]. Thus by taking the time derivative of the GOES SXR, the contribution of the trend can be suppressed and the output treated as HXR. It is important to consider how taking the time derivative of the data affects the distribution of data in resulting power spectra; it can be seen rigorously in Pugh et al. [2017b] that by taking the time derivative an additional factor of  $h^{-2} \sin^2 \omega$ , where  $h$  represents the time cadence of the data and  $\omega$  dictates the angular phase of the data

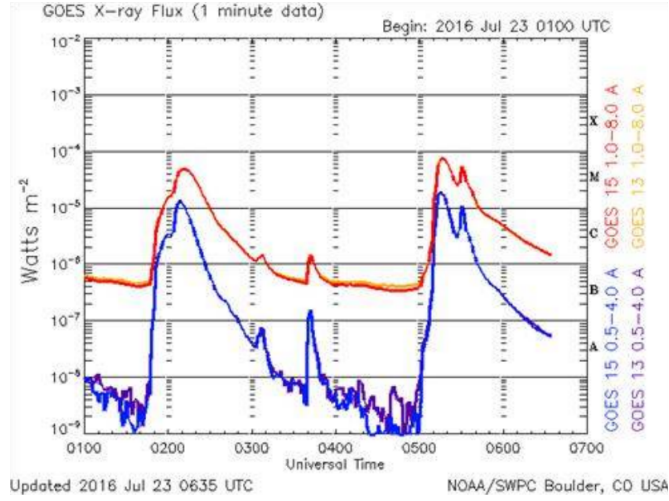


Figure 2.1: As seen in this GOES flux graph for an event on July 23<sup>rd</sup> 2016, the red curve corresponds to 1–8 Å channel and shows a slower decay of intensity following a flare at 01:40 UT. The 0.5–4 Å channel given by the blue curve shows a rapid increase followed by a sharp drop in intensity. *Image courtesy of the NOAA’s Space Weather Prediction Center.*

which ranges from 0 to  $2\pi$ , is present in the resulting Fourier spectra. This additional term has not been factored into the work contained in this thesis as this effect is most pronounced where  $\omega$  is close to 0 or  $\pi$ ; instead the first and final few datapoints that correspond to these values of  $\omega$  are omitted from analysis. The time derivative in this thesis has been approximated via the basic three-point finite difference, given as:

$$\dot{x}_n = \frac{x_{n+1} - x_{n-1}}{2h}, \quad (2.1)$$

where  $n$  is the index of the data array and datapoints are denoted by  $x$ .

### 2.1.3 *Fermi*

Solar data was also collected by the *Fermi* satellite, owned by NASA, which was launched in June 2008 [Meegan et al., 2009] and has remained operational since. The *Fermi Gamma-ray Space Telescope*, formally known as *GLAST*, collects observations of transient sources in the high energies of 8 keV to 40 MeV through the *Gamma-Ray Burst Monitor (GBM)*. This is complemented by the satellite’s main instrument; the *Large Area Telescope (LAT)* which takes readings in the range of 20 MeV to 300 GeV though no data from this instrument was used in this project. The GBM consists of 12 thallium activated sodium iodide (NaI(Tl)) scintillation detectors (8 keV–1 MeV) and two bismuth

germanate (BGO, 150 keV–30 MeV) detectors. For burst events, two files are produced; CTIME with 8 energy channels, and CSPEC with 128 energy channels. The CSPEC data has a usual resolution of 4.096 s, increased to 1.024 s immediately after an event is detected. The energy ranges from the CSPEC data used in this thesis are distributed into the ranges 6–25, 25–50, and 50–100 keV, to complement the analysis in [Pugh et al., 2017b] as discussed in Chapter 5.

#### 2.1.4 RHESSI

RHESSI is a NASA observatory launched in 2002 which is still collecting high resolution spectroscopic data of gamma-rays of energies of 20 MeV and imaging data in SXR around 3 keV [Hurford et al., 2002]. RHESSI uses a set of 9 Rotational Modulation Collimators (RMCs) which consist of two layers of small scale grids which modulate the incoming solar radiation as the satellite rotates. As each RMC contains different slit widths, a good coverage over many energies can be collected, which are reconstructed to produce images. RHESSI rotates with a period of roughly 4 s, and this rotation leads to precession and nutation errors, the scale of which is dependent on the offset of the spin axis of the detectors and main instrument. This can lead to artificial oscillations, which are artefacts of instrumentation, being introduced into data sets. This is discussed further in Chapter 4. The spatial resolution at the X-ray energies from 4–100 keV is 2 arcseconds, ranging to 36 arcseconds for gamma-rays.

#### 2.1.5 *Vernov*

*Vernov* was a Russian satellite which provided HXR data through the Detector of the Roentgen and Gamma-ray Emissions (DRGE) instrument aboard during its solar-synchronous orbit from July to December 2014 [Myagkova et al., 2016]. The satellite used four detectors with identical properties based on thallium activated sodium iodide (NaITl) and thallium activated caesium iodide (CsITl) phoswitch detectors. Phoswitch detectors record low energy X-rays, gamma rays of low intensity and may pick up alpha and beta radiation in high energy ambient backgrounds. Data from *Vernov* was analysed to complement the analysis completed in [Pugh et al., 2017b] outlined in Chapter 5. This instrument lacked spatial resolution but provided good sensitivity and energy resolution and so still produced data well suited to be analysed for QPPs.

## 2.2 Data analysis techniques

### 2.2.1 Fourier analysis

Throughout Chapters 2–5 the Fast Fourier Transform (FFT) was used as the comparative technique against EMD due to its reputation as a widely used and well respected method that is often used in programming language IDL to decompose a signal into a set of harmonic functions. A traditional Fourier transform converts data in the time domain, i.e. a signal of amplitude against time, into the frequency domain as seen in Figure 2.2. This is done by breaking down the signal into its sinusoidal components, each with unique frequency, phase, and magnitude. The conditions of these components is that they must be independent, and when all summed up must exactly reproduce the original waveform. In addition the input data must be strictly periodic or stationary and the system must be linear, otherwise any resulting spectrum will make little physical sense. These components can then be visualised in a power spectrum, which plots the power of each sinusoidal component against their frequency. For an infinite perfectly sinusoidal input signal with only one frequency, this would result in a peak in the resulting power spectrum that resembles the Dirac  $\delta$ -function. For more complex signals, a series of peaks may be seen in a power spectrum of varying amplitude. Confidence intervals may then be added so as to better ascertain which frequencies are statistically significant and which may be attributed to noise. A power spectrum produced from an FFT traditionally shows a 2D graph of power spectral density (which applies to signals existing across all time) against frequency. This expresses how the power in the signal is distributed against the sinusoidal components, which can be summed up to reproduce the original signal. Similarly a periodogram can be produced which has similarities with the power spectrum produced by an FFT, but is optimised for unevenly time-sampled data and gives significant periodicities. An example of a Fourier power spectrum may be seen in Panel 4 of Figure 2.4.

FFT is a common realisation of the Fourier transform, as it is more computationally efficient [N. Bracewell, 1989]. FFT can be carried out much faster than a Fourier Transform as it reduces the number of calculations needed to analyse the input signal of  $n$  units, from  $n^2$  to  $\frac{n}{2} \log_2 n$ . The disadvantage of this method is that its best performance is reached when the length of the data is precisely  $2^k$  units long, where  $k$  is any positive integer. This results in the usual solution of zero-padding, in which arrays of zeros are added before and after the input data so that the number of elements of the array to be analysed is exactly  $2^k$ . The correct application of FFT requires the start and end points of the waveform to reach the same value so that a whole number of periods

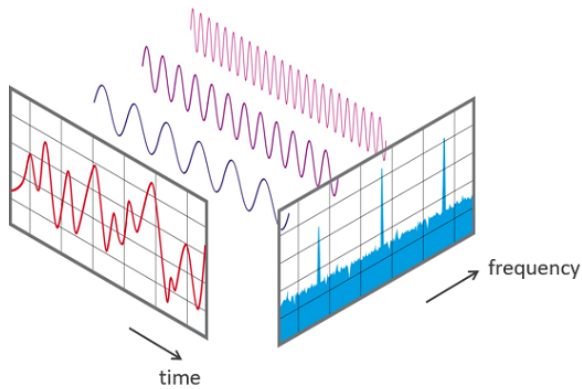


Figure 2.2: A visualisation of how the FFT algorithm breaks down a signal into several sinusoidal components which are visualised in a Fourier power spectrum. *Image courtesy of Wikimedia Commons.*

are present in the signal so as to obtain an accurate output of frequencies. This can be accounted for via a window weighting function, which minimises the resulting spectral leakage. A number of window weighting functions are available, where each offer their own trade-offs between peak sharpness and spectral leakage. A windowed Fourier transform is performed by taking the product of the input signal with some window function that is localised in time, such as a Gaussian or top-hat function. Some windows are artificially imposed on a long lasting signal to produce a waveburst, whereas some data already has the form of a wavepacket and so no additional window may be necessary for the analysis. These windows can be centred upon the section of the wave exhibiting the behaviour of interest, leading to a higher spectral resolution near the frequency of interest in the resulting Fourier spectrum. As a higher number of oscillations (or equivalently Q-factor) leads to a sharper, more localised, spectral peak in the Fourier spectrum, a compromise must be made between suppressing noise or irrelevant data and allowing the signal sufficient cycles to produce a meaningful signal. As the FFT algorithm decomposes a signal into individual sinusoidal components, it is poorly equipped to find any non-stationary signals that are observed. Thus FFT is a powerful technique for finding underlying periodic oscillations but perhaps not an appropriate method when looking for QPPs of a non-stationary nature (this is further discussed in Section 5.2).

### 2.2.2 Wavelet analysis

Wavelet analysis was also employed during this thesis. Although it is a well-established and computationally efficient technique, it suffers the same shortcomings as Fourier anal-

ysis when it comes to non-stationary data. Wavelet transforms hold an advantage over FFT where wavelets are localised in time and frequency whereas Fourier only has a frequency localization. Windows are similarly exploited in wavelet analysis as mother-functions, or motherwavelets, and do not have to be confined to real space. Just as in the windowed Fourier transform, there is no ideal solution to picking a motherwavelet; only more appropriate choices to make in terms of the motherwavelet for different data sets. The motherwavelets will cycle through several iterations both on the time and frequency domain, and so can have short temporal widths for higher frequencies and larger temporal widths for low frequencies, allowing the wavelet to pick up on the evolution of multiple frequencies over time (see Torrence & Compo [1998] for a more in depth description of wavelet analysis). Compared to the Fourier transform, wavelet analysis is more computationally intensive as it provides extra resolution via the visualisation of period drift. During this project many preliminary iterations of wavelet analysis were carried out with different motherwavelets, both real and complex, but the method was deemed to be poorly equipped to accurately analyse QPP signals. This is because, although wavelet analysis is able to detect slowly varying non-stationarity, the drift of QPP parameters is comparatively fast and so is often missed when using wavelet analysis [Dennis et al., 2017].

### 2.2.3 Empirical Mode Decomposition

EMD was first proposed in Huang et al. [1998] as a method of analysing non-linear and non-stationary time series. The method has remained largely unchanged and works by decomposing a data set into a finite number of intrinsic mode functions (IMFs). This technique, which is entirely empirical and self consistent, is adaptive and works with the instantaneous time scale of the data and hence can handle non-stationary and non-linear data well, unlike Fourier and wavelet analysis (see Table 2.1). EMD has previously been applied to a wide range of data sets which contain non-stationary signals, such as seismological studies [Loh et al., 2001] and solar physical data [Nakariakov et al., 2010]. This thesis examines the use of this technique upon both artificial and real QPP candidates.

The method can be described in two stages; firstly the decomposition which breaks down a signal into several IMFs, and secondly the creation of an EMD spectrum which is used for assessment of the statistical significance of the detected IMFs in comparison with white and coloured noise. The decomposition is largely dominated by a sifting process, which relies on several key parameters, namely the *shift factor*,  $\epsilon$ , and

the *maxsifting* values, each of which will be discussed.

	Fourier	Wavelet	EMD
Basis	A priori	A priori	A posteriori adaptive
Presentation	Energy in frequency space	Energy in time-frequency space	Energy in time-frequency space
Non-linearity	No	No	Yes
Non-stationarity	No	Yes	Yes
Feature extraction	No	Discrete; Yes. Continuous; No.	Yes
Theoretical base	Complete mathematical theory	Complete mathematical theory	Empirical

Table 2.1: Comparison between Fourier, wavelet and EMD analysis. *Adapted from Huang & Wu [2008].*

### Intrinsic Mode Functions

The method of EMD breaks down a complex signal through a sifting process, into a residue and a set of IMFs. IMFs are waveforms in the time domain which may represent sinusoids, but equally may carry non-harmonic forms. Similarly to how a Fourier transform breaks a signal into sinusoids that can be summed to recreate the original waveform, IMFs form a complete basis for the input signal (alongside a monotonically increasing or decreasing residue). An IMF can be identified when it fulfils two criteria;

- The number of zero crossings and the number of IMF extrema should differ by no more than one,
- At any point of an IMF the mean envelope should equal zero.

Thus a family of IMF functions can be found, with each successive IMF decreasing in mean modal oscillatory frequency. Hence the last IMF obtained has the largest time-scale and usually corresponds to the trend of the data, which can be deducted from the initial data set as a proxy for detrending. If the trend is multi-modal, it may be attributed to a number of low frequency IMFs that can be summed together. The highest frequency IMF is also discounted from the analysis even if it lies above confidence intervals as unlike higher modes it does not show the normal distribution of instant amplitudes even for a pure noisy signal [Kolotkov et al., 2016]. These IMFs can be represented graphically using the Hilbert transform on a so-called Hilbert spectrum (see Figure 2 in Kolotkov et al. [2015] for an example) and may have varying frequency and amplitude over time, contrasting to a signal acquired by Fourier analysis.

## Sifting Process

The IMFs are identified during a procedure known as a ‘sifting process’. Raw data is taken in and detrended by an initial decomposition in which the lowest frequency mode is identified and fitted against the data. If this mode can be taken to be a good fit for the trend, it is deducted from the raw data to produce a detrended signal, if not the decomposition process is repeated using new values for the shift factor until a good fit is found. If the data is already without an obvious trend or has been detrended via other methods this step can be skipped and the data can be carried straight through to the sifting. During the sifting, signals that have been obscured by noise can be filtered out as follows:

1. Identify local maxima and minima of data,
2. Construct upper and lower envelopes via cubic spline interpolation,
3. Construct mean envelope,
4. Subtract the mean envelope from the data,
5. Check whether this new data fulfils IMF criteria, if not repeat steps 1-5.

Once a valid IMF has been found, it is deducted from the data and the procedure is repeated until a stopping criteria is fulfilled. There are several proposed criteria for the stopping of the sifting process, the most instinctive of which is predefining the sensitivity of the decomposition via fixing the value of the standard deviation between two subsequent siftings. The standard deviation, taken to be the shift factor, is defined as follows [Huang et al., 1998]:

$$Shift\ factor_k = \sum_{t=0}^T \frac{|g_{k-1}(t) - g_k(t)|^2}{g_{k-1}^2(t)}. \quad (2.2)$$

Here,  $k$  is the index representing the number of sifting iterations carried out so far,  $g$  is a ‘proto-IMF’, such that following fulfilment of the stopping criteria it can be called an IMF. The shift factor is predefined around 0.2, but can be reduced to values as small as  $10^{-3}$  in some cases, and may exceed 1.5 in rare circumstances. The extracted IMFs are highly sensitive to the value of the shift factor and so choosing an appropriate value requires a comparison of extracted IMFs with significant periodicities found using other spectral techniques, in this case Fourier or wavelet analyses. By using both methods to complement one another, the resulting global EMD spectrum allows assessment of the significance of IMFs and their associated mean modal frequencies (where here the

term modal refers to an intrinsic *mode* function, rather than a modal average). By analogy with the global wavelet spectrum, a global EMD spectrum differs from an EMD spectrum by averaging the instantaneous periods of the individual IMFs, ridding it of its time-dependence. Thus all references to EMD spectra are, in truth, global EMD spectra, but this distinction will be dropped for ease of reading. Other parameters that govern the sifting process are  $\epsilon$  and *maxsiftings*. The value of  $\epsilon$  dictates the lowest modal amplitude allowed for an IMF, which has been set to  $10^{-3}$  in the code used during the analysis carried out in this thesis. Should the modal amplitude slip below this level the sifting automatically terminates. The maximum number of siftings to be carried out before termination of the process to prevent over-sifting is given by *maxsiftings*, and is usually given the prescribed value of  $10^4$ . Following the fulfilment of the stopping criteria, the lowest frequency IMF would be sifted out and the remaining signal, known as the residue, is entirely monotonic such that no further IMFs can be extracted.

### Confidence intervals

For results obtained by any signal analysis it is important to apply confidence intervals so statistically significant results can be obtained and their properties examined. Although the techniques for implementing confidence intervals on Fourier power spectra differ from EMD spectra, the underlying principle remains the same. As defined in Kolotkov et al. [2016] noisy components on a Fourier spectrum can be seen to follow a power-law spectral energy distribution, where their ‘colour’ can be represented by the variable  $\alpha$ , according to relation

$$S = Cf^{-\alpha}, \quad (2.3)$$

where  $S$  is the spectral power density,  $f$  is frequency, and  $C$  is an arbitrary constant that can be put to unity for convenience and  $\alpha$  gives the degree of correlation (colour) in the noise.  $\alpha = 0$  corresponds to entirely non-correlated (white) noise,  $0 < \alpha$  is red/coloured noise and  $\alpha < 0$  corresponds to blue noise which is rarely observed in solar data. When  $S$  and  $f$  are plotted on a logarithmic graph,  $\alpha$  can be extracted as the gradient via simple mathematical manipulation of Eq. 2.3. Thus for most cases we can assume there are two sources of noises, as in the results of Pugh et al. [2017b], one can immediately be assumed to be white and the other coloured to an unknown degree,  $\alpha$ , the value of which can be fitted via the data. A broken power-law can be fitted with a zero gradient for high frequencies where white noise dominates and a coloured component for lower frequencies following a variable ‘breaking point’. Through use of the IDL *Periodogram.pro* program, an offset at a predefined confidence level according to the false alarm probability can be

found, and simply summed to the fitting of the data. Thus the peak of highest power may cross these boundaries and is deemed to be significant to the given level, i.e. it can be said with a given probability that this signal is not produced by random noise. During the projects put forward in this thesis, the confidence intervals were chosen to be 95% and 99%. Thus for a 95% confidence interval, it can be said that the likelihood for a peak, which appears above this interval, to be randomly generated through noise is 5%.

For EMD, the analogous equation of Eq. 2.3 is defined in Kolotkov et al. [2016] as

$$E = C' P^{\alpha-1}, \quad (2.4)$$

where  $E$  is the mean modal energy,  $P$  is the mean modal period,  $\alpha$  is defined as before and  $C'$  is a new constant once again arbitrarily reduced to 1. As before, on a logarithmic plot of  $E$  and  $P$  (which will later be shown to be an EMD spectrum in Figure 2.3), the value for  $\alpha$  can be extracted as  $\alpha = \text{gradient} + 1$ . Once again a broken power-law can be fitted to the data, with one gradient fixed according to  $\alpha = 0$  in the region of high frequency where white noise dominates, and another in the lower frequency region where coloured noise dominates and the gradient is a free parameter. Using this fitting, we can extract a value for a breaking point, and for second gradient in the region of low frequency. In both the Fourier and EMD spectra, if  $\alpha$  remains equal to zero throughout and no coloured component can be discerned from the data, this will be reflected in the fitting.

Unlike Fourier analysis, the false alarm probability offset method cannot be applied to EMD spectra as the data follows a chi-squared distribution with the numbers of degrees of freedom varying across the spectrum, and with the colour of noise. Instead using techniques from Kolotkov et al. [2016] we can find the confidence intervals according to a chi-squared distribution of energies  $E_m$  that correspond to specific IMFs.

$$f(E_m) = \frac{k_m}{\bar{E}_m} \chi^2 \left( \frac{k_m E_m}{\bar{E}_m}, k_m \right), \quad (2.5)$$

where the parameter  $k_m$  represents the number of degrees of freedom and  $E_m$  the modal energy density, which has a dependence on the associated instantaneous period and index  $\alpha$ . Confidence intervals are found for each value of  $\alpha$ , giving upper and lower boundaries, of which significant modes lie outside. For the results where the two values of  $\alpha$  are prescribed, two confidence levels (corresponding to 95% and 99%) are given for each value of  $\alpha$ , producing overlapping regions as seen in Figure 2.4. This is simplified in Figure 2.5 and subsequent results, where only the upper bounds of the 95% and 99%

confidence intervals are given for each value of  $\alpha$ , making significant IMFs easier to identify. Here the assumption has been made that no significant IMFs of real origin are observed beneath the lower confidence intervals, as IMFs in this region are of extremely low amplitude, and therefore the lower confidence intervals are omitted in these figures.

#### 2.2.4 Interpreting an EMD spectrum

Figure 2.3 shows a simplified EMD spectrum generated from an artificial input signal. The black signal in Panel 1 shows the waveform that has been created via a summation of two stationary sinusoids (with periods of 2 and 5 s) combined with low amplitude white noise. These two harmonic components have been reconstructed as IMFs via EMD and can be seen in red and blue with decreasing frequency. The EMD spectrum in Panel 2 represents these two IMFs, each shown as a single dot plotted as their mean period against their modal energy and are colour coordinated to their counterparts in Panel 1. The confidence intervals appear as solid lines where red is 95% and green is 99% and the dashed line represents the mean energy across the range of periods. The IMFs that correspond to the input sinusoids in Figure 2.3 all lie well above the 99% confidence level due to the high signal to noise ratio. Any IMF can be represented by a single point on an EMD spectrum and re-expressed in the time domain for comparative purposes. The black dots seen in the EMD spectrum correspond to modes associated with noise, and as they lie below both confidence intervals are statistically insignificant.

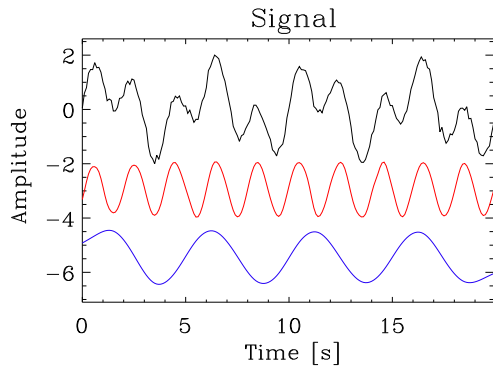
#### Analysis of a signal with two prescribed noisy components

Figure 2.4 shows a signal where a noisy component of  $\alpha = 1.5$  is prescribed. The original simulated signal (with a period of 10 s) summed with a trend and with noise in Panel 1 is shown as a solid black line, where the dashed line indicates the prescribed trend and the green line representing the trend found via the EMD method. This signal has been detrended via deducting the EMD obtained trend, as shown in the second panel where again the prescribed signal is indicated by a dashed line, and the extracted IMF is given in red. The third panel shows the EMD spectrum, with the orange and light green solid lines corresponding to the 95% and 99% confidence intervals for white noise respectively, and similarly for the red and green solid lines of the coloured noise. The dashed lines indicate the fitting by modal energies of the IMFs to their periods from which the values of  $\alpha$  are found. The IMFs are represented by blue bullet points, and the significant mode, shown as a red diamond, corresponds to a period of 9.85 s which is again significant above the 99% level.

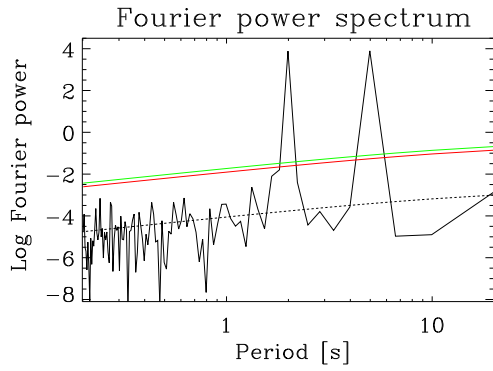
It can be seen that the ‘breaking point’ between white noise and coloured noise dominated data occurs at a period corresponding to  $\approx 1.1$  s. This means that all modes for periods smaller than 1.1 s should be treated as white noise dominated fitting, similarly for coloured noise for periods greater than 1.1 s. Note how the breaking point of the confidence intervals (i.e. where the confidence intervals due to coloured noise become greater than the confidence intervals for white noise) does *not* necessarily correspond to the same period of the ‘breaking point’ of the fitting. The period corresponding to the breaking point of the confidence intervals can be seen to be greater than that of the model’s breaking point. This relatively crowded plot is simplified in future spectra by taking the upper bounds of the dominating confidence level either side of the *confidence interval’s breaking point*. Thus for Figure 2.4, the 99% is given by the upper light green confidence interval (generated by the fitting of dominated white noise data) until the confidence interval breaking point wherein it hits the upper green confidence interval (generated by the fitting of dominated coloured noise data). This is combined into a piecewise function that can be seen in all EMD spectra to follow. This is repeated for 95% confidence intervals. Panel 4 shows the Fourier spectrum of the detrended signal, where a significant peak at 9.97 s which peaks above the 99% confidence interval can be seen. As a result of the two noise components, a broken power-law can be seen in the Fourier spectrum and the resulting confidence intervals.

### **Analysis of a signal with a non-prescribed alpha**

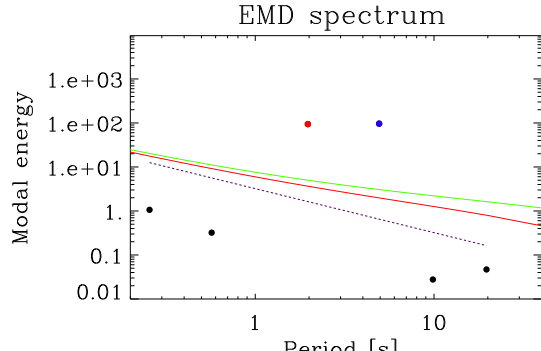
Figure 2.5 shows a simulated signal as before but originates from a ‘black box’ such that no information about the periodicity of the underlying QPP is given, nor the properties of any noise obscuring it. Here, the confidence intervals in the EMD spectrum (Panel 3) have been simplified, showing only the upper bounds. This is the manner in which all subsequent confidence intervals will be displayed for EMD spectra in the projects to come. Figure 2.5 shows decent agreement between the Fourier and EMD spectrum which both see oscillations of similar periodicities. However the Fourier spectrum isolates one periodicity of 16.5 s whereas the EMD spectrum shows a decomposition of the signal into two statistically significant modes of 12.7 and 18.5 s, above the 99% confidence interval. The combination of these two modes can be seen overlayed in red in Panel 2, showing very good agreement with the input signal. This is a good example as to where Fourier and EMD do not converge to the same period and this project will explore the reasons behind the discrepancies and examine in which situations it is more appropriate to use one over the other.



(a)



(b)



(c)

Figure 2.3: A signal in the time domain, generated as the sum of two sinusoidal components of periods 2 (red) and 5 s (blue) and randomly distributed white noise, can be seen as a black curve in (a). The two sinusoidal components have been recovered via EMD and the IMFs are displayed. Their spectral peaks can be seen in the Fourier power spectrum (b) and shown in the EMD spectrum in (c) as the corresponding coloured bullet point. Statistically insignificant IMFs are shown as black bullet points in (c).

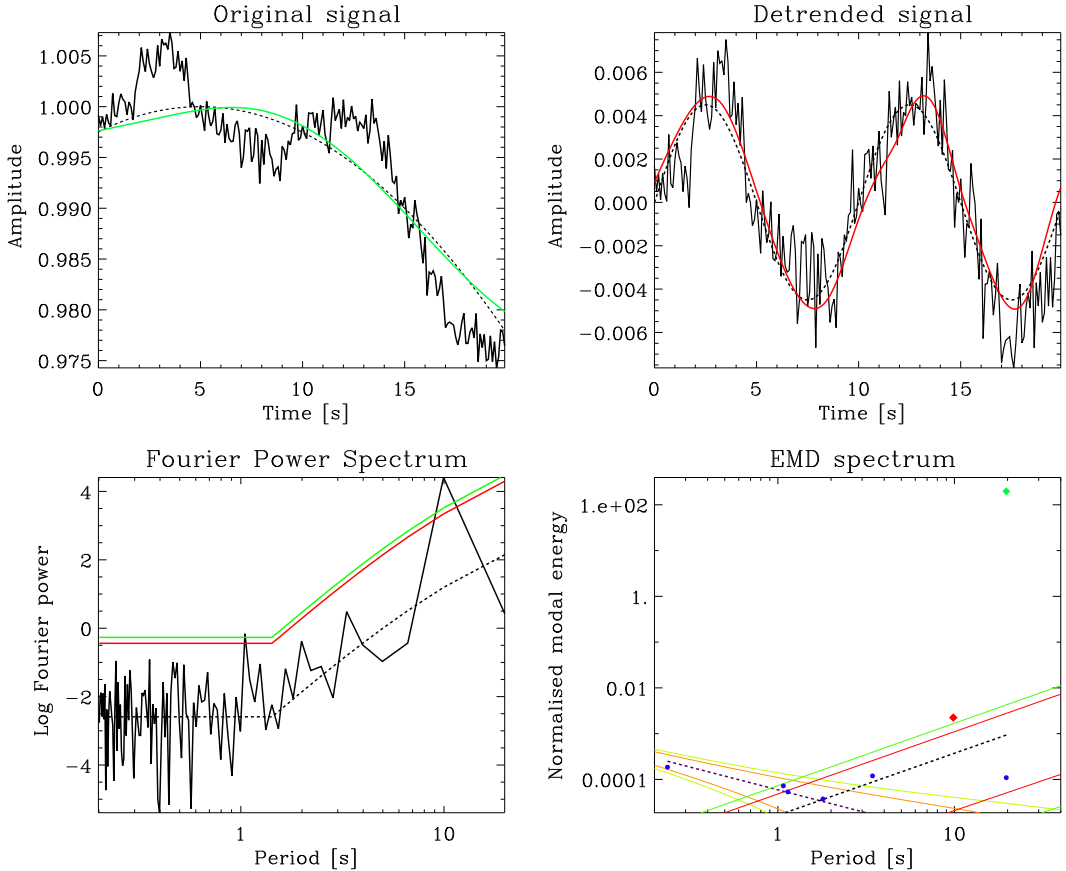


Figure 2.4: Clockwise from top-left; Panel 1: Profile of a synthetic noisy signal with an embedded oscillation of 10 s (solid black). The dashed black line is the prescribed trend, and the EMD extracted trend is shown overlayed in green. Panel 2: Detrended signal via trend found using EMD, shown in solid black. The prescribed oscillation is shown as a black dashed line, and the EMD extracted significant IMF is shown in red. Panel 3: EMD spectrum of the raw input signal. Two IMFs, seen as diamonds, can be seen above the confidence intervals (coloured solid lines). The non-significant IMFs are shown as blue bullet points, the significant IMF (shown as a red solid line in Panel 2) is given as a red diamond with a mean period of  $\approx 10$  s, and the trend (seen in green in Panel 1) is given as a green diamond with a mean period of  $\approx 20$  s. The two gradients of the sets of confidence intervals relate to the two values of  $\alpha$  seen in the raw data. Panel 4: Fourier spectrum of the detrended signal, with a fitting showing a flat region with  $\alpha = 0$  dominating over high frequencies and an inclined region for  $\alpha > 0$  with one significant peak seen at  $\approx 10$  s which compliments the results of the EMD spectrum. The black dashed line gives the fitting of the data to a broken power-law, from which the confidence intervals (solid red and green lines) were generated.

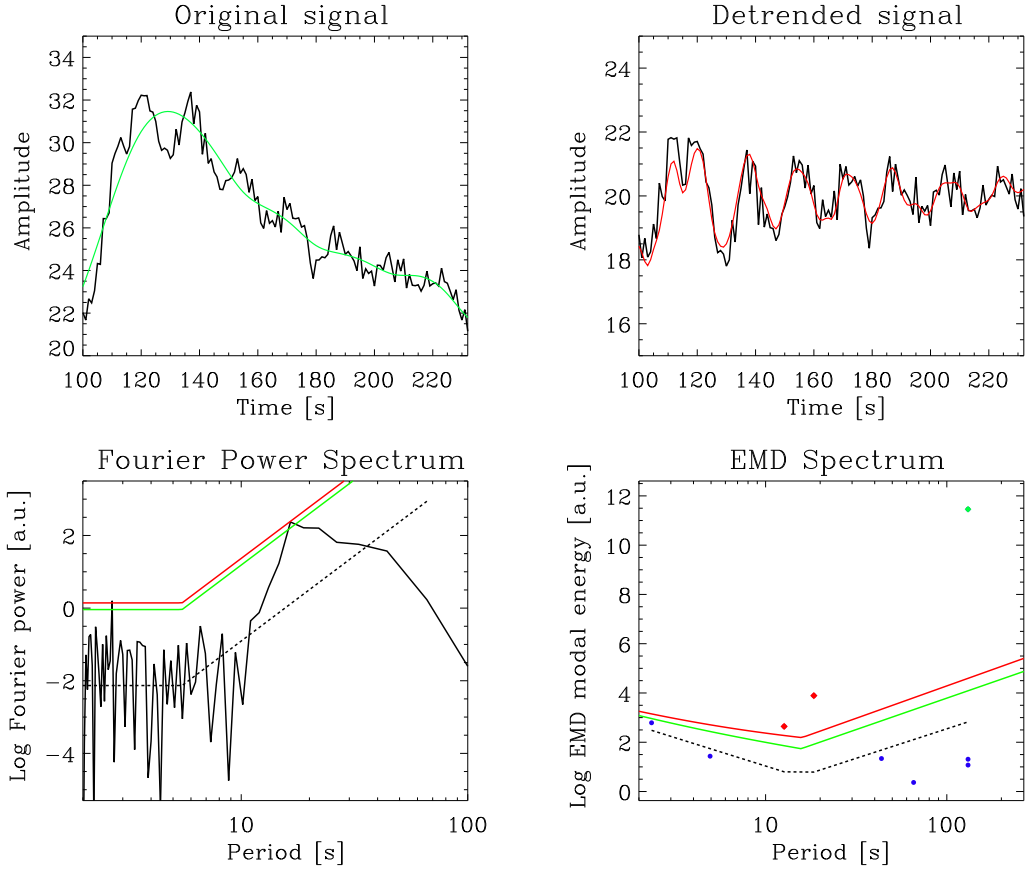


Figure 2.5: Clockwise from top-left; Panel 1: Raw synthetic signal with an oscillation of unknown period trimmed to focus on the impulsive and decay phase of the flare (solid black). The trend extracted by EMD is shown overlayed in green. Panel 2: The detrended signal, overlayed with the sum of the two significant IMFs, shown in red. Panel 3: EMD spectrum. As in Panel 2, the green and red solid lines indicate confidence levels of 95% and 99% respectively. The blue bullet points represent insignificant IMFs, whilst two significant modes above the 99% level are seen with mean periods of 12.7 and 18.5 s, represented by red diamonds. The trend is seen as a green bullet point, representing an IMF of high energy. Panel 4: The Fourier spectrum of the detrended signal. Dashed black line indicated the fitting via a broken power-law. The confidence intervals are indicated as in Panel 3. A significant peak above the 95% interval is seen at  $t \approx 16.5$  s.

# Chapter 3

## Hare and Hounds exercise

### 3.1 Introduction

In this chapter, a Hare and Hounds exercise is introduced, wherein flare light curves (of both simulated and real origin) were analysed using different techniques to search for QPPs. The aim of this exercise was to find the strengths and shortcomings of several popular well-established and newer techniques for the detection of QPPs.

### 3.2 Creating the flares

For this exercise 100 flares were simulated, following either an exponential or Gaussian shape in the decay phase. The exponential shape was based on the work put forward by Davenport et al. [2014] wherein a profile following a two stage exponential decay was proposed. This allows for a quick initial decay which slows as time increases, mimicking the behaviour exhibited by solar flares observed in the high energies. A restriction of this model is that a sharp peak is not necessarily observed. The second model instead uses two half-Gaussian curves: one (with a quicker rise) giving the rapid increase of intensity for the rise phase of the flare; and a second with a larger width to give the slower decaying region. This allows for a broader peak, which is advantageous as QPPs have been seen to occur during the peak of the flare.

The flare shapes, offsets, amplitudes and duration of the flare, alongside the parameters dictating the rates of rise and decay of the flares (e.g.  $\sigma_{rise}$  for the Gaussian based flares) were allowed to vary randomly according to a uniform distribution, and the datasets were given a randomly generated numerical label for identification. A small number of flares with non-standard properties were created and inserted into the

datasets; four events contained two QPP signals and a further four events contained non-stationary QPPs, evenly shared between the Gaussian and exponential flare shapes.

The majority of QPP signals were generated as sinusoids, modulated by a decaying exponential, with randomly generated variable parameters, such as the phase and period. Such a model has been previously used for both solar and stellar data as seen in Pugh et al. [2016]. In the few cases where two QPP signals were present, the second QPP had a smaller amplitude than the first, and the decay time and period were scaled relative to the first. For the non-stationary signals, the QPPs' form follows that of stationary signals, but the frequency was varied according to the logarithmic chirp function;

$$\nu = \nu_0 \left( \frac{\nu_0}{\nu_1} \right)^{\frac{t}{t_1}},$$

where  $\nu$  governs the frequency, and  $\nu_0$  is defined as  $(\text{input period})^{-1}$  and  $\nu_1$  is the frequency at some time predefined  $t_1$ . The QPP signals were obscured by randomly generated noise of varying colours. White noise was determined from a Gaussian distribution where  $\sigma$ , the standard deviation, was determined relative to the flares amplitude, and as the QPPs amplitude was governed by the flares amplitude, this meant that the white noise is proportional to the QPPs' amplitude. Red noise was added to the datasets and computed as follows:

$$N_i = rN_{i-1} + \sqrt{(1-r^2)}w_i,$$

where  $N$  gives the red noise element,  $w$  denotes the white noise component taken from a Gaussian distribution and  $r$  dictates the correlation coefficient between adjacent noise elements. Power-law distributed noise is commonly observed in solar and stellar flare time series and can lead to false detections which are better attributed to the trend of the data. Therefore red/coloured noise had to be carefully excluded from analysis to limit the number of false detections. Background trends, either linear or quadratic, were also overlayed onto the signals. In addition, a small number of flares of real solar or stellar origin were added to the dataset and rescaled and renamed in order to make them indistinguishable from the artificially generated signals.

### 3.3 Detection methods

Several different techniques were employed during this exercise and were based on a periodogram approach in the majority of cases, as seen from a sample of methods shown in Table 3.1. Chapter 3 follows the use of EMD, referred to as Method 2 from here

Description		References
Method 1	Periodogram based significance testing	[Vaughan, 2005], Pugh et al. [2017b]
Method 2	Empirical Mode Decomposition (EMD)	Kolotkov et al. [2016]
Method 3	Smoothing and fitting to a model followed by generation of a Lomb-Scargle Periodogram.	Doorsselaere et al. [2011]
Method 4	Wavelet Analysis with the Morlet mother-function	[Torrence & Compo, 1998]
Method 5	Automated Flare Inference of Oscillations (AFINO)	[Inglis et al., 2015], [Inglis et al., 2016]

Table 3.1: A selection of the methods employed in Hare and Hounds Exercise 1, alongside a brief description of their bases. Further description of the techniques can be found in the associated references or in Broomhall et al. [2018].

onwards, in Hare and Hounds Exercise 1.

Figure 3.1 shows the typical output given by analysing a flare using Method 2, which employed EMD, Fourier analysis and a construction of a wavelet spectrum for comparative purposes. Figure 3.1 shows Flare 58618 — a flare of simulated origin, shown to have a non-stationary oscillation following the impulsive phase of the flare. The instantaneous period can be seen to grow, as seen in the wavelet spectrum of the statistically significant IMF (Panel 3). The periodogram (Panel 2) shows a rather broad peak with no statistically significant components above the 95% or 99% confidence interval, which is as to be expected for analysis of a non-stationary signal using methods which assume the signal to be harmonic. The EMD spectrum (Panel 4) shows the intrinsic mode detected above a 99% confidence interval as a red diamond, which can be seen explicitly as the black lightcurve in Panel 3, and in red overlayed on the original lightcurve (black) in Panel 1. The trend shown as a green diamond is seen in green in Panel 1. The wavelet spectrum, only used for visualisation of the period drift in the mode identified with EMD, was produced using a Morlet motherwavelet on the intrinsic mode extracted via EMD (Panel 4) and shows a growth in instantaneous period with time. The overlayed white line shows the approximation of the obtained period-time dependence by the chirp function.

Using Method 2, 26 flares were analysed with all showing some significant oscillations. It transpired that although many of these detections matched well with input parameters, there were a number of false detections where EMD had detected quasi-

periodic behaviour that arose due to red noise. These high amplitude detections blurred the boundary between red noise and trend, resulting in difficulty for an observer to distinguish between trend and oscillation. Another key difficulty to note regarding EMD in the Hare and Hounds exercise was the relatively time consuming nature of the technique. As discussed in Section 2.2, EMD is sensitive to the choice of shift factor and requires manual input for each iteration. This limited the number of flares that could be analysed in a given time compared to other methods employed in this exercise (e.g. Methods 1 and 3, as shown in Figures 3.2a).

### 3.4 Summary

Figure 3.2 shows a selection of results from Hare and Hounds Exercise 1 (for results of Hare and Hounds Exercise 2, where the signal to noise ratio was reduced, see Broomhall et al. [2018]), with input periods plotted against the periods recovered via a variety of methods. There was a wide range in the accuracy of the different results, with Method 1 outputting the most highly correlated results across a large range with many datasets (as seen in Figure 3.2a). Similarly Method 3 produced a well correlated set of results (see Figure 3.2c). Based on these results it can be suggested that for the majority of cases where these methods obtain a period, it will be reasonably close to the input period. However as previously mentioned, both Methods 1 and 3 rely on techniques assuming a stationary and harmonic input and so did not pick up the four non-stationary signals as Method 2 did, as seen in Figure 3.3. In Hare and Hounds Exercise 1, the four non-stationary signals were only detected using Method 2, and the detected periods agreed well with the input period of the chirp function. Therefore it would be sensible to suggest using Fourier-based methods based on stationary inputs where the signal exhibits no period-drift (which could be ascertained via a quick production of a wavelet spectrum as in Panel 3 of Figure 3.1). In the cases that a drift is seen, the signal should instead be passed on to Method 2 or a similar signal analysis technique which is designed to specifically handle non-stationary signals.

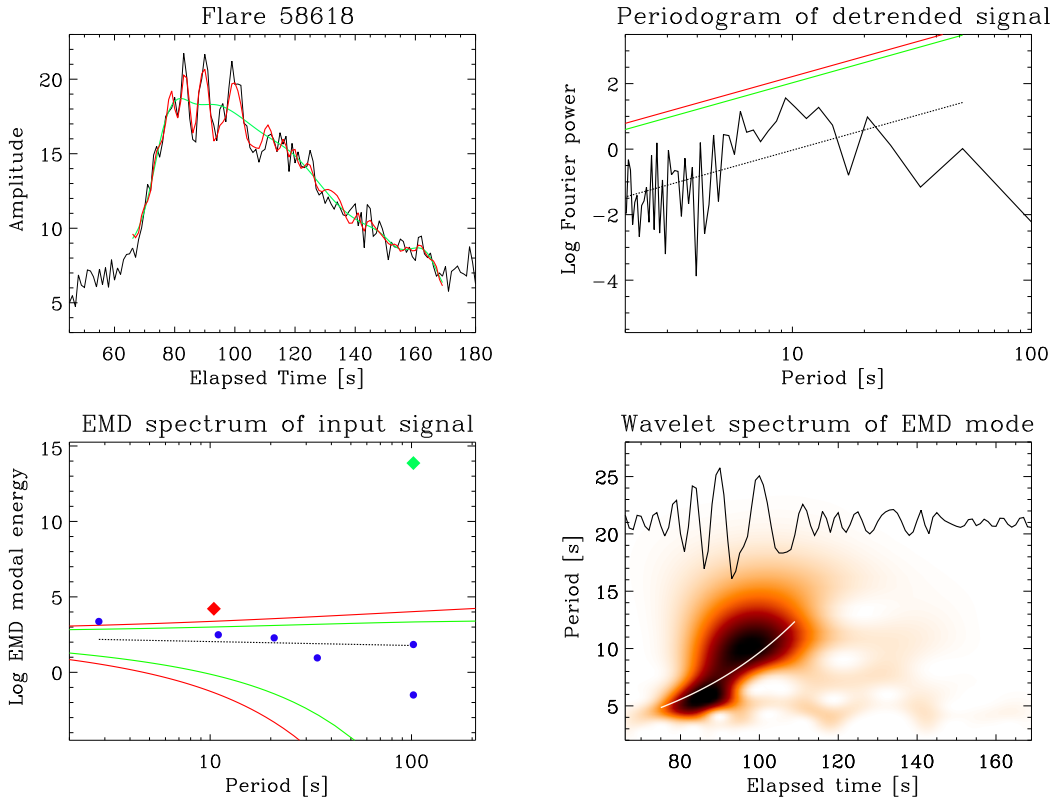
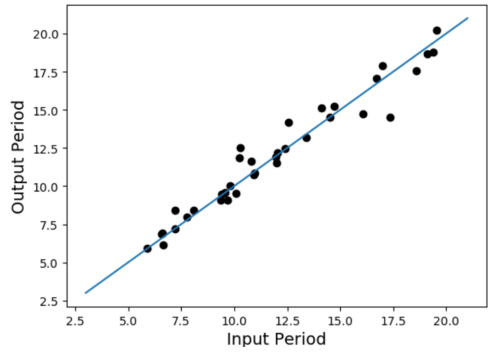
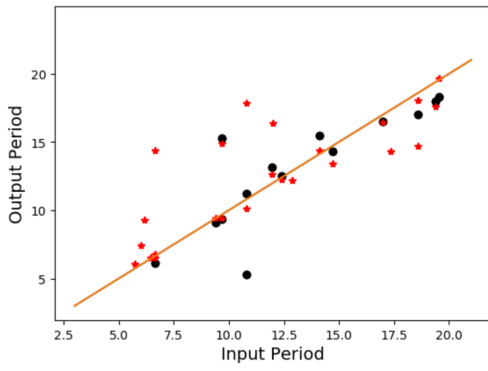


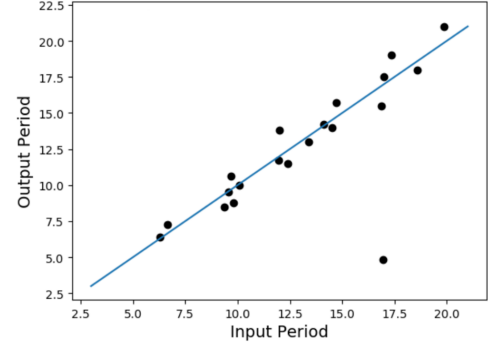
Figure 3.1: Clockwise from top-left. Panel 1: Trimmed profile of Flare 58618 in black with the EMD extracted trend shown in green, and the trend and significant mode combined signal shown in red. Panel 2: Periodogram of the detrended signal where the 95% confidence interval is shown as a solid green line and 99% in red. Panel 3: Morlet wavelet spectrum of the significant intrinsic mode found (shown as a black solid line, represented as a red diamond in Panel 4). Panel 4: EMD spectrum of original input signal with significant mode shown as a red diamond. The trend is given as a green diamond. Blue circles correspond to insignificant IMFs, where  $\alpha \approx 0.89$ . The 95% and 99% confidence intervals are given by the green and red lines, respectively, with the expected mean value shown by the dotted line.



(a) Method 1



(b) Method 2



(c) Method 3

Figure 3.2: A selection of results for Hare and Hounds Exercise 1. The coloured lines shown in Panels (a), (b) and (c), show perfect agreement between in the input and output period, i.e. if a datapoint lies on this line, the method that was employed found the ‘correct’ output period such that it agrees perfectly with the input period. Thus, more accurate methods have a greater correlation of datapoints with this line. In Panel (b), the stars give the results acquired by EMD, and the black bullet points give those found by Fourier analysis on a detrended signal.

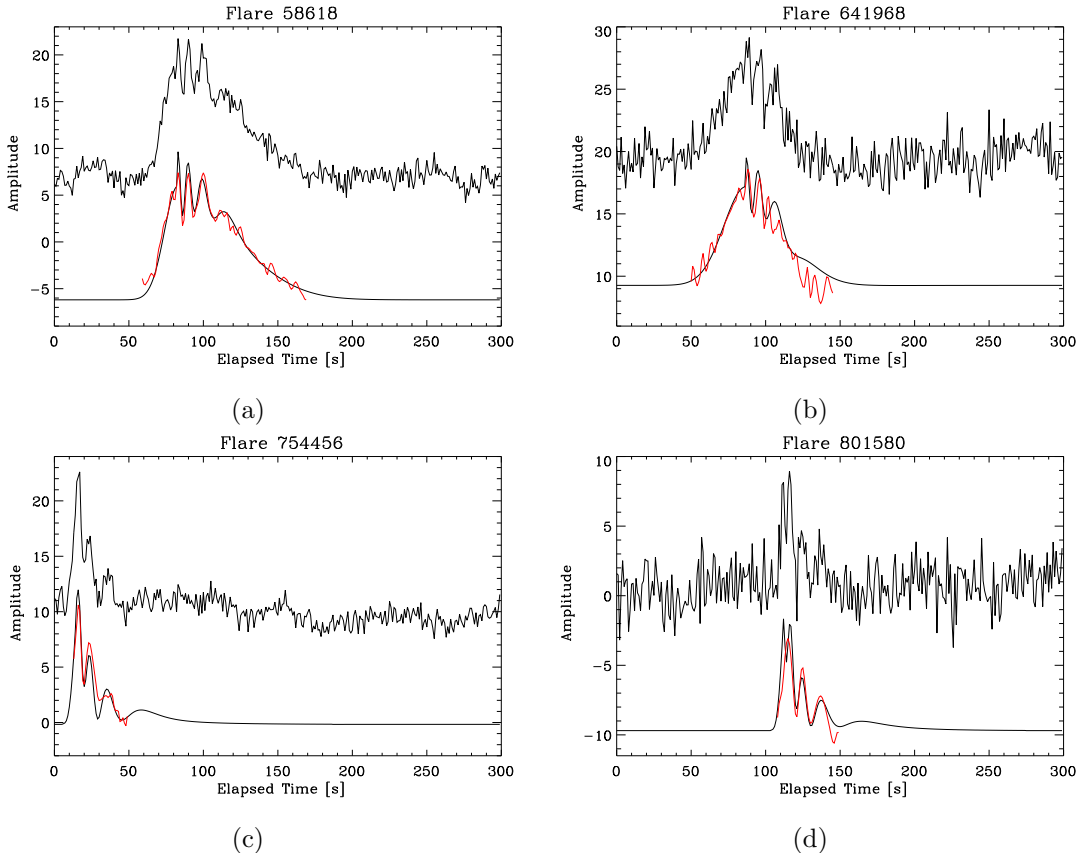


Figure 3.3: Comparison of statistically significant IMFs from EMD analysis of the four non-stationary signals in Hare and Hounds Exercise 1. Each panel shows an untrimmed raw lightcurve as a solid black line. Below the lightcurve is the input model with all coloured and white noise removed, containing a trend and non-stationary signal, which was obtained following the analysis for comparative purposes. Overlayed onto the input model is the intrinsic mode function of the (manually selected) flare phase, shown in red. For the cases of Flares 58618, 641968 and 754456, it was unknown to the author that the signals were of non-stationary origin and were hence analysed blindly. Flare 801580 was analysed separately in the knowledge it contained a non-stationary signal.

## Chapter 4

# Investigating hard X-ray sources at flaring loop footpoints

### 4.1 Introduction

Using the EMD technique outlined in Section 2.2, seven regions of interest were analysed to look at HXR sources in candidates for a ‘magnetic zipping’ mechanism as discussed in Zimovets et al. [2018], Liu et al. [2009]. This mechanism describes a configuration where a magnetic flux rope (MFR) or filament, is situated above an arcade and erupts from its anchored position from one side of the arcade. This sudden asymmetric eruption is akin to the motion of a whip and hence is also known as a ‘whipping’ motion. As the MFR stretches the first loop of the arcade above the magnetic polarity inversion line (MPIL) upward, an X-point may emerge below the MFR due to magnetic tension creating conditions suitable for magnetic reconnection (see Figure 4.1 for an illustration of this mechanism). This magnetic reconnection accelerates impulsive electrons to the footpoints of the loop causing rapid release of high energy HXR concentrated at the footprints. As the MFR continues to erupt, loops will continue to undergo magnetic reconnection one after another and the HXR sources will appear to travel parallel to the MPIL. As the loops making up the arcade are largely independent structures, the rate of release of HXR from their footpoints would be dependent on properties of the emergence of the MFR and so would not be required to obey any periodic pattern and would appear randomly distributed in time. In this chapter, we will examine whether the erupting MFR model agrees with RHESSI data analysed with EMD and discuss the presence of artefacts from instrumentation error.

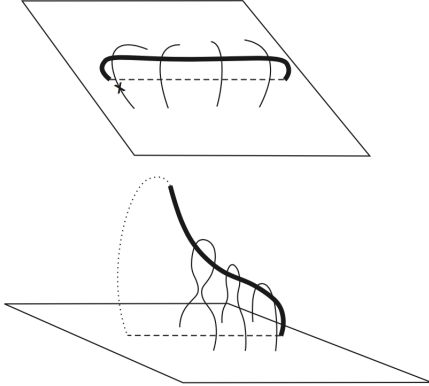


Figure 4.1: An asymmetric eruption of a filament (thick loop) in a whipping motion, ‘unzipping’ an overlying arcade (thin loops). The dashed line indicates the position of the MPIL. *Image taken from Liu et al. [2009].*

## 4.2 Data analysis

The data analysed was obtained by RHESSI, and contained an array of counts per second per detection with a 4 s time step. Seven events were analysed, corresponding to the flares examined in Zimovets et al. [2018]. All events were analysed in the 50–100 keV band, which corresponds to HXR, in order to see if the several bursts of HXR seen display any hidden periodicity. If so, this may indicate a common driver for the release of HXR. A lack of evidence of this would lend support to the hypothesis that these HXR bursts are caused by a whipping or unzipping mechanism as put forward in Liu et al. [2009]. For the seven events, no statistically significant IMFs were observed above a 95% confidence interval, other than one event in the fourth dataset corresponding to an event on April 18<sup>th</sup> 2014, which gave an oscillation with a mean period of 78.3 s, as seen in Figure 4.2. The implications of this specific period are discussed in Section 4.3. The recovered values of  $\alpha$ , the parameter representing the degree of correlation between datapoints for noise, ranged between 1.2–3.0 for the seven datasets.

## 4.3 Errors arising due to procession and nutation in the RHESSI spacecraft

As there is an offset of alignment between RHESSI’s spin axis and imaging axis (which can vary in magnitude depending on magnetic torquing), artificial oscillations may appear which can be incorrectly identified as having solar origin (see Inglis et al. [2011]).

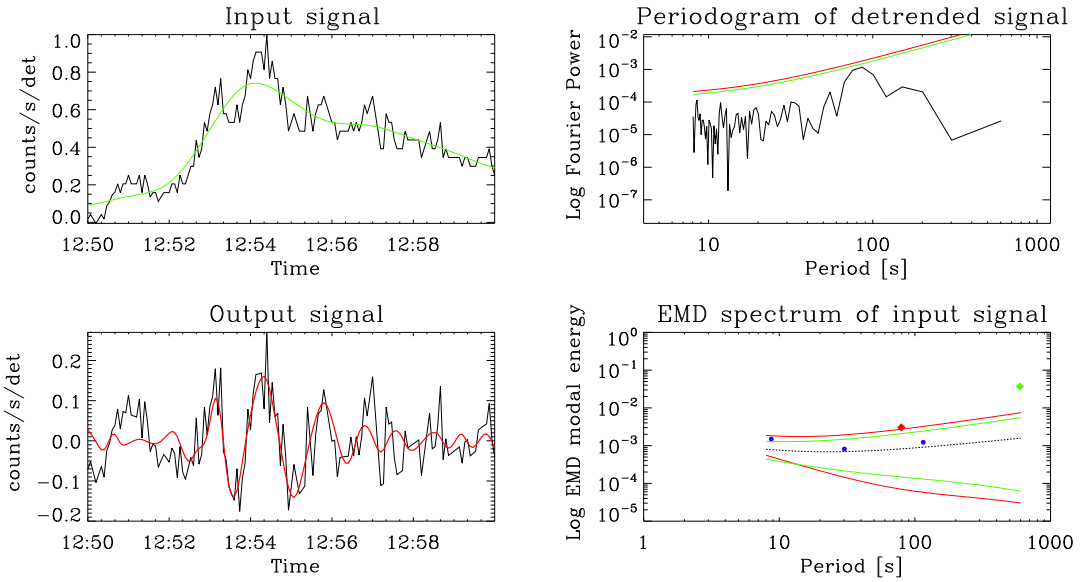


Figure 4.2: Event #4 SOL2014-04-18 showing a significant oscillation of 78.3 s, analysed similarly to Figure 2.5.

This false periodicity is known to be in the range of 75–80 s, wherein the extracted period falls, as seen in Figure 4.2. Thus this significant oscillation of 78 s was carefully examined. As the RHESSI craft rotates with a period of approximately 4 s or equivalently 15 rmp (see Section 2.1), the craft will be impacted by precession and nutation effects which can lead to misinterpretation of data. The nutation errors, caused by a misalignment between the detector and the craft’s spin axis forces the flux of X-ray photons to be modulated correspondingly through to the subcollimators of the craft. As each of RHESSI’s detectors are aligned on their own axis, this effect varies detector to detector. In particular Detector 5 holds the greatest sensitivity to this effect as its axis carries the greatest offset, and evidence of this oscillation can be seen in Figure 4.3. Usually this effect is more commonly seen in the lower energy channels, up to 25 keV, however for this particular event it seems it is significant enough to be seen in the 50–100 keV waveband. As the periodicity of the significant IMF lies firmly in the region associated with this error, and an evidence of an artificial oscillation can be seen in Figure 4.3, with reasonable confidence this mode can be associated with a RHESSI artefact.

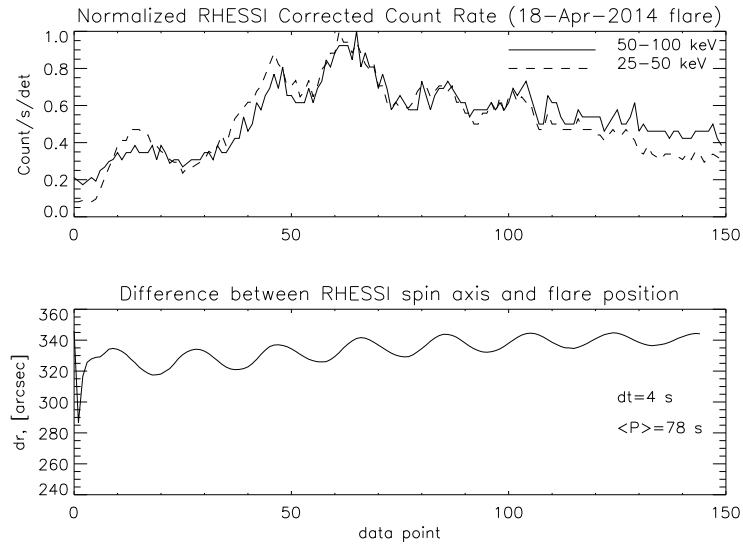


Figure 4.3: Evidence of an underlying oscillation due to nutation with a period of 78 s  
*Figure courtesy of I. Zimovets.*

## 4.4 Summary

All seven flares present no significant oscillatory behaviour in the energy band of 50–100 keV that can be attributed to solar origin according to EMD (nor in the analysis performed by Kuznetsov et al. [2016] which was based on both wavelet and Fourier analysis). Thus it is reasonable to consider that these irregular pulsations of HXR may be independent events, possibly associated with the action of a zipping mechanism. It is important to stress that a lack of evidence of statistically significant oscillations is insufficient to conclude that these oscillations do not exist. Further research should be undertaken to investigate this, with emphasis on observational data to look for evidence of a buoyant flux rope. This research would include an exploration of these curves in different energy bands, 6–12 keV and 20–50 keV, to see if there is a lack of periodicity in the thermal emission which would encourage confidence in the erupting MFR mechanism for these seven events. Moreover, useful information could be provided by the study of the progression of the HXR kernels along the MPILs. There are an additional 22 flares given by Kuznetsov et al. [2016] in which the irregular pulsations of HXR sources appear to independent events, which has yet to be confirmed in SXR.

## Chapter 5

# Quasi-periodic pulsations observed in a single active region

### Introduction

A recent paper [Pugh et al., 2017b] claims that 55 flares within a single active region showed evidence of QPPs with reasonable confidence of 95%. During this analysis, which was carried out using Method 1 as discussed in Chapter 3, observations were taken from a number of instruments, namely; GOES/XRS, Extreme ultraviolet Variability Experiment (EVE) aboard SDO, *Fermi*/GBM, *Vernov*/DRGE and NoRH. This active region was observed for more than three Carrington rotations from September to November 2014 and was classified with three distinct NOAA identifiers: 12172, 12192, and 12209. The aim of this project was to compare the use of EMD in detecting QPP candidates and reveal possible scaling between observational parameters of QPPs. Similarly to Chapter 3, the method outlined in [Pugh et al., 2017b] will be referred to as Method 1, and the technique of EMD will be referred to as Method 2. In this chapter we will contrast the results found by Method 1 and Method 2 and suggest a cause for the cases where the results of the two methods strongly disagree. In addition we will examine a short survey of flares where an apparent modulation between instantaneous amplitude and period is seen and discuss the implications this may have on the mechanisms put forward which may drive QPPs.

## 5.1 A comparison of analysis techniques

### 5.1.1 Data analysis via generation of a periodogram

For Method 1 the QPPs were detected via creation of a periodogram of the time series data, with QPP candidates flagged if a peak above a 95% confidence interval was seen. The confidence intervals were constructed taking into account the presence of red noise and data uncertainties via the method outlined in Pugh et al. [2017a] which is in turn based on a test put forward by Vaughan [2005].

A confidence level of 95% would correspond to a false alarm probability of 5%, i.e. for a spectral peak lying above such a level there is a 5% chance that the signal is created by some combination of noise. Thus it would be inaccurate to say that a signal exists with 95% certainty, rather there is a 5% likelihood that it appears as an artefact of chance. So the confidence level corresponding to spectral peak lying above a specific false alarm probability  $\gamma_{\epsilon_j}$  can be expressed as:

$$Pr\{\hat{\gamma}_j > \gamma_{\epsilon_j}\} \approx \frac{\epsilon_{N'}}{N'}, \quad (5.1)$$

where  $\epsilon_{N'}$  is the false alarm probability and  $N'$  is the number of datapoints in the power spectrum (this is discussed further in Pugh et al. [2017a]). However for a regular power spectrum which follows a chi-squared distribution with two degrees of freedom this changes the probability distribution to a far more complex integral. Furthermore, as the datasets investigated by Method 1 were rebinned for the purposes of better assessing the power from a peak that spans multiple adjacent frequencies, the distribution of noise was altered. This once again led to modifications in the appropriate method of creating confidence intervals, and is explained in full in Pugh et al. [2017a].

### 5.1.2 Results and discussion

Of the 181 flares looked at originally by Method 1, there were 55 detections of statistically significant oscillatory behaviour: 36 from GOES; 8 from NoRH; 6 from *Fermi*; 3 from *Vernov*; and 2 from EVE. It is important to note that these are not necessarily unique events, as an observation of the same event temporally in different channels of the same instrument has been recorded as two distinct events. Of these 55, the 2 events seen by EVE were arbitrarily discarded due to time constraints and the remaining 53 events were analysed using Method 2.

The procedure followed in Method 2 used to analyse the candidates is outlined in Section 2.2. Confidence levels of 95% were chosen so results could be directly compared

to the results from Pugh et al. [2017b]. A full table of results can be seen in the Appendix A. Of the 53 flaring events looked at by Method 2, 44 events were seen to exhibit oscillatory behaviour at a significance of 95% or above. Of those 44 events, 32 oscillations showed agreement between the two methods of detection, where agreement was defined for the two periods to be within 5 s of each other (indicated by the shaded region in Figure 5.1). Thus the success rate of a QPP seen to agree by both Methods 1 and 2 was 32/44, i.e. 73% across the four instruments: NoRH; *Vernov*; *Fermi*; and GOES.

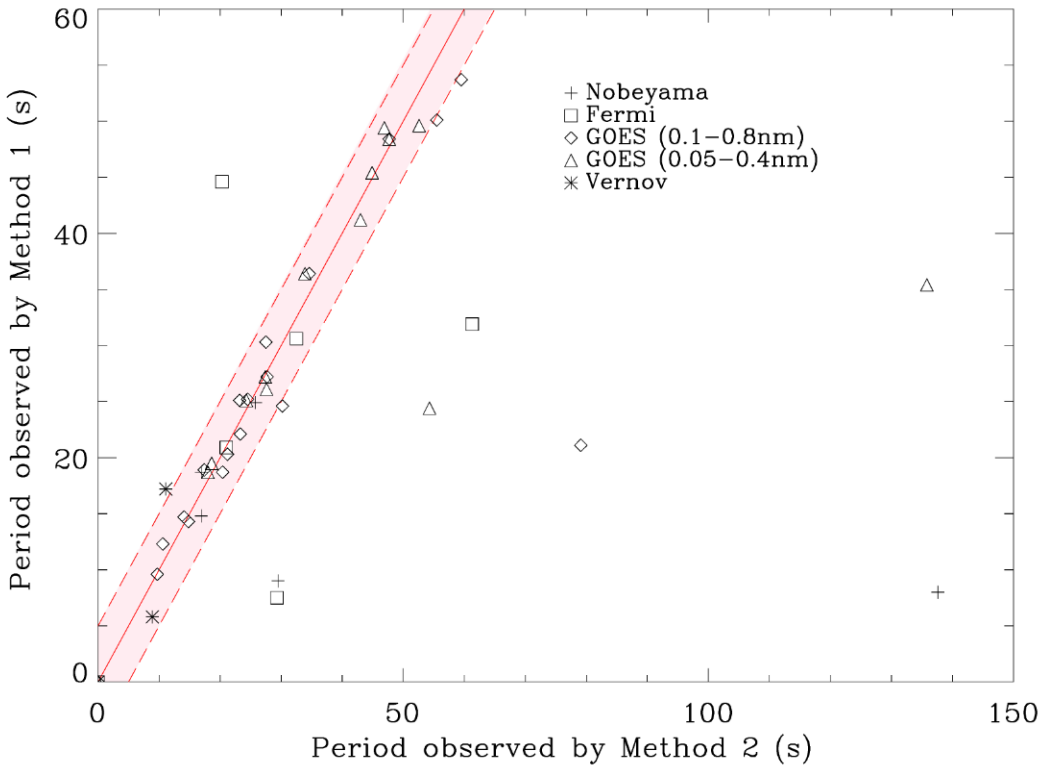


Figure 5.1: A comparison of observed periods using Methods 1 and 2. The solid red line indicates perfect agreement of the same observed period, and the datapoints that lie within the shaded region correspond to QPP candidates where the periods found by Methods 1 and 2 are within 5 s of each other.

Whilst for 73% of the events the measurements agreed reasonably well, there were several events where the observed mean periods differed greatly. One such example can be seen in Figure 5.2, labelled in the Appendix as the second measurement corresponding

to Event 38 which took place at 04:20 UT on the October 19<sup>th</sup> 2014. This event was allocated a period of 24.4 s using Method 1 (see Figure 5.3), and 54.3 s using Method 2, which clearly does not give good agreement. The original signal can be seen in the top-left panel of Figure 5.2.

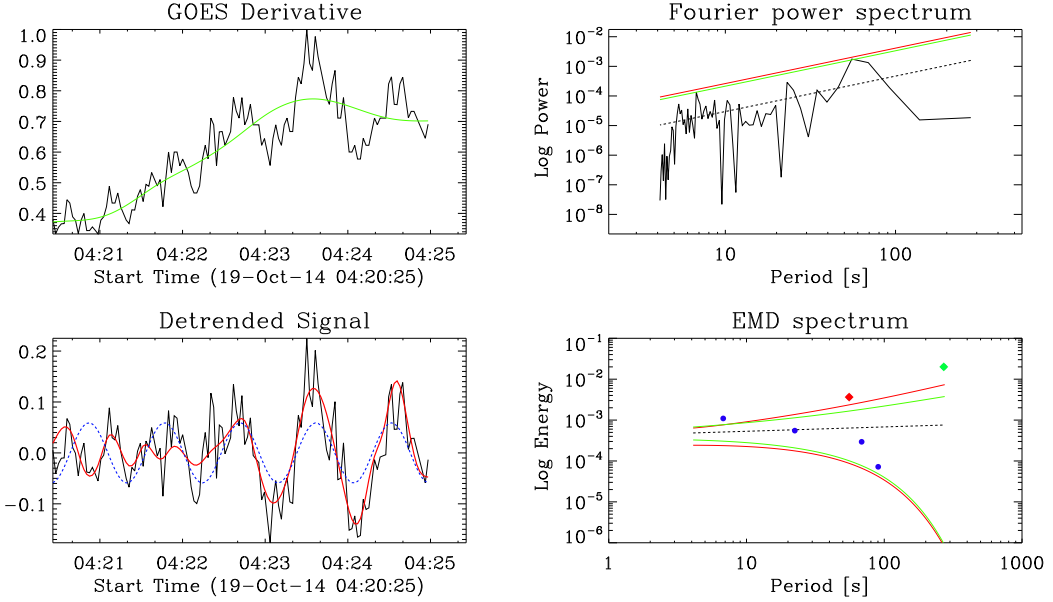


Figure 5.2: Similar to Figure 2.5 with GOES/XRS data in the 0.5–4 Å channel for event SOL2014-10-19T04:20. Panels are labelled clockwise from top left. The significant mode is shown as a red diamond in the EMD spectrum, Panel 3, and has a mean period of 54.3 s. Panel 4 gives the detrended signal (black), overlayed with the significant IMF (red) and the Fourier extracted oscillation (blue, dashed).

The origin of this discrepancy between the two methods may lie in the characteristics of the light curve. As seen, both the amplitude and the period of the signal can be seen to change during the oscillation and this non-stationarity of the signal cannot be picked up by Fourier based techniques such as Method 1, as discussed in Section 2.2. To illustrate this, the significant peak in the Fourier power spectrum (seen in Panel 2 in Figure 5.3, at approximately 55 s) has been composed to reproduce the oscillation, shown as a blue dashed line in Panel 4. This oscillation is stationary and so its phase matches poorly with the input signal for several cycles, and its amplitude remains constant despite the input signal growing in amplitude. Contrastingly, the significant IMF (shown in red), exhibits a growing amplitude and period during the course of the signal, displaying a better correlation with the input signal.

This effect was seen in a number of other events during this survey where a growing or shrinking period has caused a significant discrepancy between the recorded periods. Given the 73% agreement rate of the two methods, it seems reasonable to consider Method 2 as a technique to find significant oscillations in solar data. Particularly in the cases of non-stationary signals where there is disagreement between the two methods, the data should be further analysed for evidence of period drift and evaluated further by the more appropriate method. Future research could combine the two methods, detrending the signal using IMFs found through Method 2 and then using the relatively fast and accurate Method 1 in cases where the data can be seen to be of stationary origin. This may help decrease the number of false detections originating from the trend and red noise.

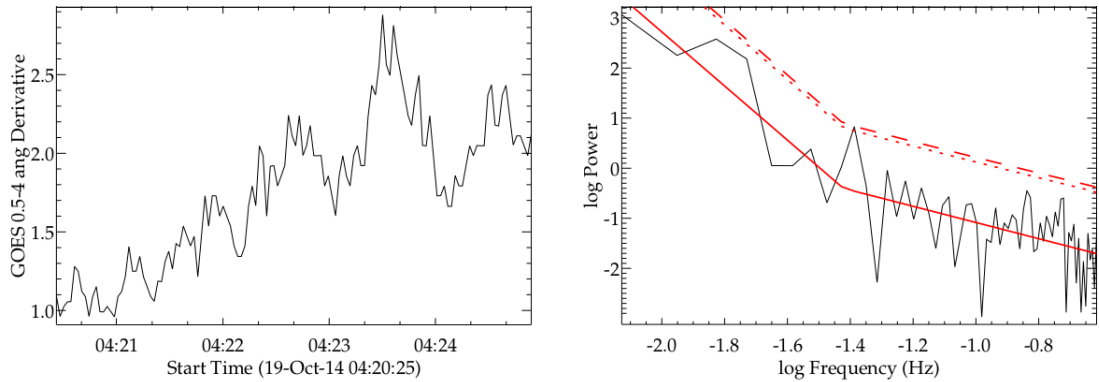


Figure 5.3: The spectra produced by Method 1 for the event SOL2014-10-19T04:20. The left panel gives the light curve in the GOES 0.5–4 Å channel. The right panel gives the corresponding power spectrum where the solid red line is a broken power law fitted to the data, and the dotted and dashed lines represent the 95% and 99% confidence intervals respectively. The peak in this power spectrum corresponds to a period of 24.4 s. *Figure adapted from Pugh et al. [2017b].*

## 5.2 Scaling of QPP properties

### 5.2.1 Motivation

As discussed in Chapter 1 it is currently unknown which generation mechanism(s) create QPPs due to insufficient data, though a number of candidates have been put forward. As each mechanism predicts different observable properties, by looking at the characteristics of the QPPs the mechanisms may be backwards engineered, leading to a better

understanding of the processes guiding solar behaviour. Section 5.3 follows a small survey on 11 QPPs (of which 10 appear from the active region discussed earlier in Section 5.1) to see if they exhibit any relationship between their periods and amplitudes and to what degree. Positive results of this survey would lend confidence to a repetitive regime of spontaneous magnetic reconnection, also known as magnetic dripping.

Magnetic dripping refers to a load/unload mechanism wherein magnetic energy may be compared to a fluid dripping under the competition of surface tension and gravity. The size and frequency of the drops are guided by the force of gravity, surface tension and the inflow rate of the fluid, and a higher frequency would correspond to smaller drops and vice versa, provided the inflow rate and surface tension remain the same. Analogously magnetic energy can be considered to be provided by a continuous inflow, concentrating toward the epicentre of a flare and ‘dripping’ out in a quasi-periodic manner as bursts of energy. This regime, and several others are discussed in greater detail in Nakariakov et al. [2010]. This particular mechanism would thus produce QPPs where the amplitude of the intensity of the energy burst would scale according to the period of oscillations.

### 5.2.2 Effective quality factors of QPPs

For the 44 events described given in Section 5.1.1 where a significant oscillation (above the 95% confidence interval) was found using Method 2, the effective quality factor was measured by taking the number of oscillation cycles visible whilst the instantaneous amplitude was greater than  $\frac{1}{3}$  of its maximum value. This was also carried out for three additional flaring events originating from different active regions, one of which can be seen in Figure 5.6. This allowed for the histogram (Figure 5.4a) to be constructed, giving the number of oscillation cycles observed in each QPP i.e. an effective quality factor of the significant IMF extracted using EMD. Only a small number of oscillation cycles are typically seen in a QPP, and so QPPs may be better described as a wavelet rather than a harmonic function modulated by an envelope. In addition, as these QPP wavelets show evidence of modulation of both the amplitude and period, these QPPs are best expressed as non-stationary oscillations (see Figure 5.5, as discussed further in [Nakariakov et al., 2018].

## 5.3 Proportionality of amplitude and period in QPPs

Observation of a correlation between period and amplitude of a QPP signal would lend support to ‘magnetic dripping’ models, as discussed in Sections 1.3.1 and 5.2.1. Figure

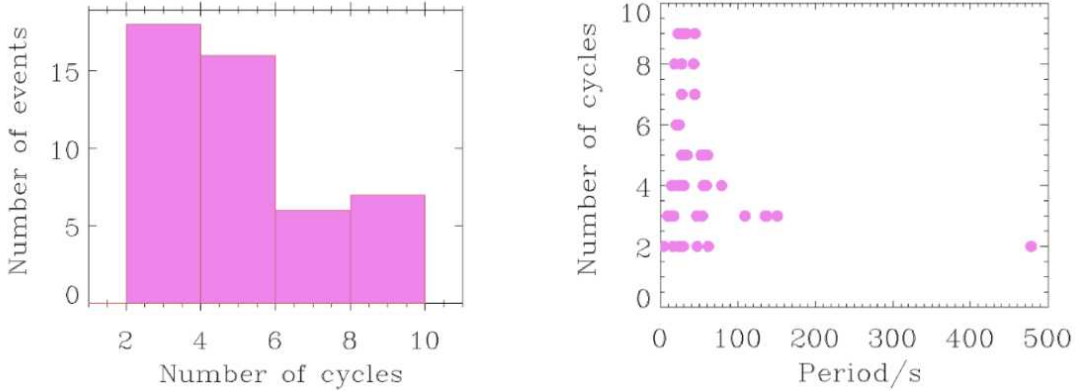


Figure 5.4: Panel 1 (Left): Histogram showing the distribution of the number of oscillation cycles seen in 44 QPPs events from active region 12172/12192/12209, as analysed in Chapter 5. Panel 2: Mean period of QPP events against the number of observed oscillations. *Both figures adapted from [Nakariakov et al., 2018].*

5.6 shows a lightcurve, where the instantaneous amplitude grows in tandem with the instantaneous period. This QPP candidate, denoted SOL2014-02-25T00:41, was recorded by Nobeyama Radio Polarimeter and analysed using EMD. Figure 5.7 was created by initially measuring the instantaneous amplitude and period at each peak and trough for a singular lightcurve, producing several data points that connected to produce one piecewise function. Thus one of the piecewise lines provides information about how the scaling of period and amplitude evolved over the wavetrain. This process was repeated for all 11 events, each differentiated by colour. Some events, such as the one indicated by a light green, showed considerable scaling, and exhibited a long period when the amplitude grew, whereas this effect was less pronounced (but still present) in the event given by an orange function. Although these are preliminary results, in need of a wider and denser dataset, this seems to suggest good evidence of a correlation between the two properties.

Furthermore it can be seen that modelling a QPP as a simple harmonic oscillator (given as Eq. 5.2) is insufficient if we take into account the scaling of QPP parameters.

$$\ddot{x} + \omega_0^2 x = 0, \quad (5.2)$$

where  $x$ ,  $\dot{x}$ , and  $\omega_0$ , classically represent the displacement, its second derivative, and angular frequency respectively. When used to model QPPs,  $x$  is used as a proxy for

signal intensity. This relation implies a solution of the form  $x = A_0 \cos(\omega_0 t + \phi)$ , with phase  $\phi$ , which would result in a constant period for any given amplitude  $A_0$ . In reality, it is known that the presence of a wave affects the medium it travels in, which in turn affects the parameters of the wave. Thus all waves have some degree of non-linearity to them, but usually the higher order terms which should be present in Eq. 5.2 (caused by perturbations in the medium) are treated as negligible. This leads to the interpretation that parameters such as amplitude are unaffected by the values of displacement, phase etc. which does not correspond to observational evidence. Hence model 5.2 is insufficient to model all QPPs and requires some modification, likely including higher order terms. This preliminary evidence of a positive correlation between amplitude and instantaneous period for a small sample of QPPs indicates that a magnetic dripping model, or a similar load/unload mechanism, may be a suitable candidate for a QPP generation regime. It should be noted that although the signals analysed in this chapter do appear non-stationary in time, we cannot confidently conclude that these wavetrains are the result of non-stationary sources. Although magnetic dripping is perhaps the most intuitive regime that could explain the apparent proportionality between instantaneous amplitude and period, it is not the only possible generation mechanism that could result in this observed behaviour. For example, a non-stationary non-linear sinusoidal wavetrain would exhibit some dependence of instantaneous amplitude on other parameters, leading to different instantaneous speeds throughout the wavetrain. Therefore as it evolves in time, the signal would tend towards a sawtooth profile, which is interpreted as a non-stationary signal. Equally, this anharmonic profile could be the result of initial perturbations of the system and as we have no time resolution to see how the wavetrain evolves in time, it cannot be confidently concluded that the signal is of non-stationary non-linear origins.

As the scaling of period and amplitude is not observed for all QPPs, it lends weight to the idea that QPPs ought not to be analysed as a whole but are instead generated through at least two regimes, one of which leads to a proportionality between amplitude and period, and one that does not. A classification system for QPPs may allow further relationships between parameters to be explored and lead towards generation mechanisms being found for QPPs. This is still a long way off however, and this survey must be carried out on a far greater sample size before any conclusions can be confidently drawn.

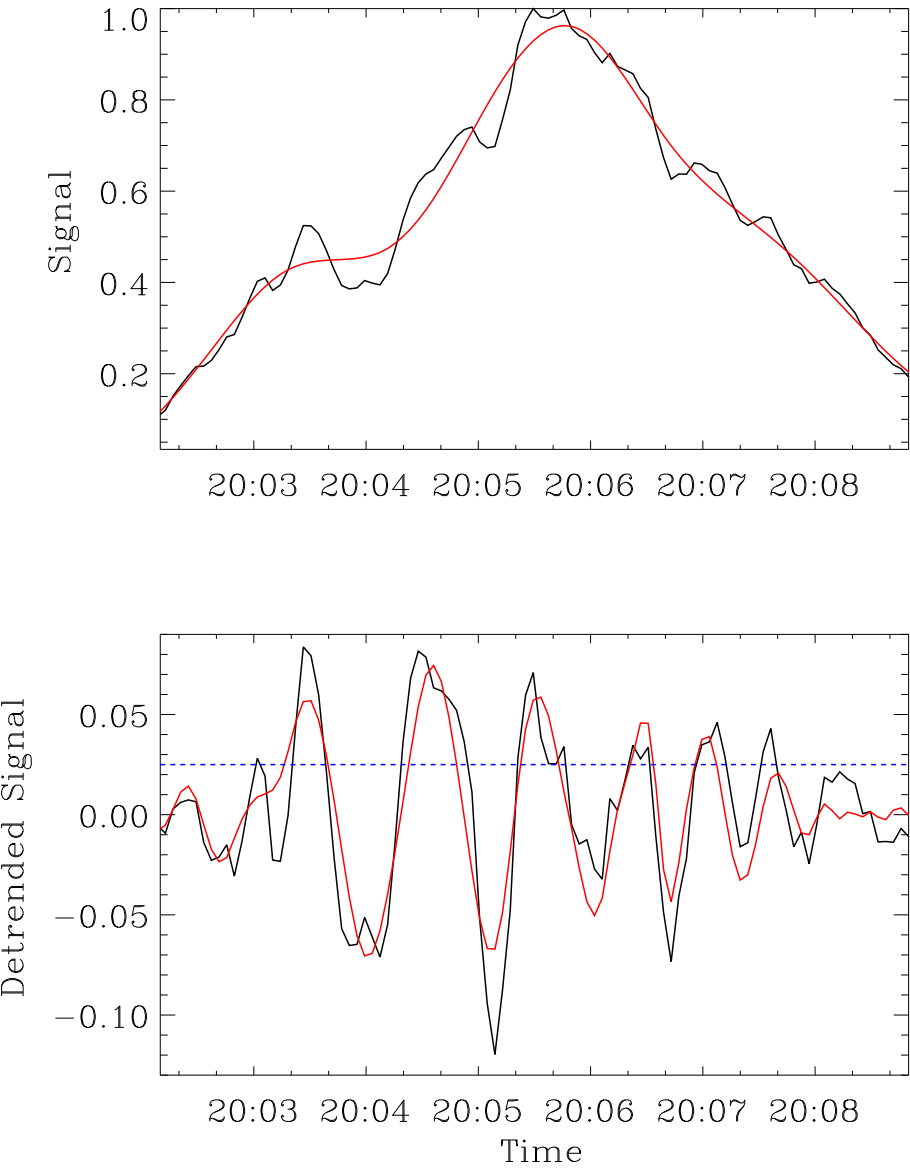


Figure 5.5: Top: In black, the non-stationary light curve for the event SOL2014-10-27T20:03 (Event 106 in the catalogue of events discussed in Chapter 5) recorded with *Fermi* in the 50–100 keV channel, where the red curve shows its trend obtained by EMD. Bottom: The detrended light curve (black) overlayed with the extracted significant mode using EMD (red). The blue dashed line indicated a third of the maximum amplitude of the intrinsic mode, so that the effective quality can be discerned. In this case, five cycles of the IMF are seen above this boundary. *Figure adapted from [Nakariakov et al., 2018].*

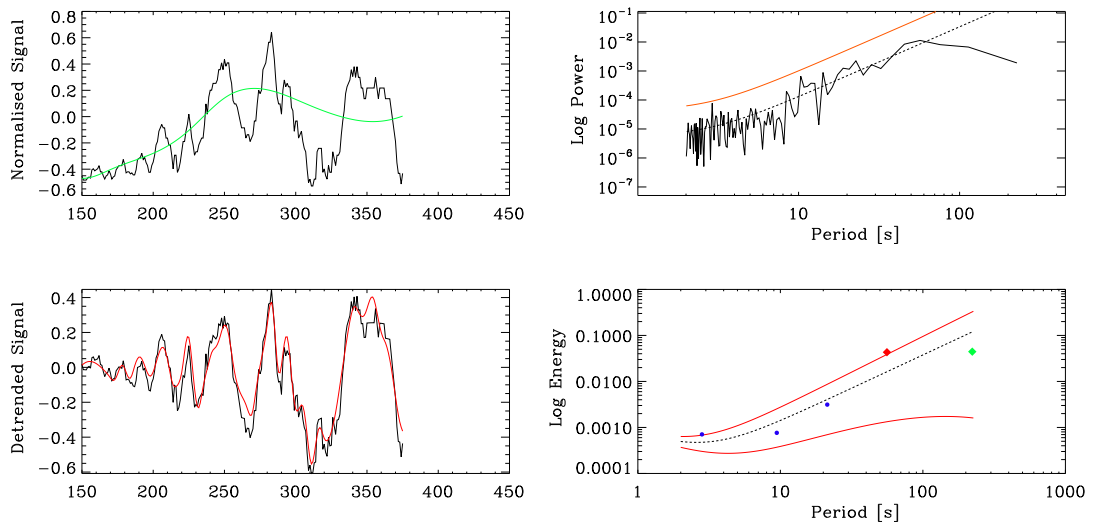


Figure 5.6: Light curve for event SOL2014-02-25T00:41, showing clear scaling between instantaneous period and amplitude, observed by Nobeyama Radio Polarimeter (NoRP) in 17 GHz, analysed similarly to Figure 2.5.

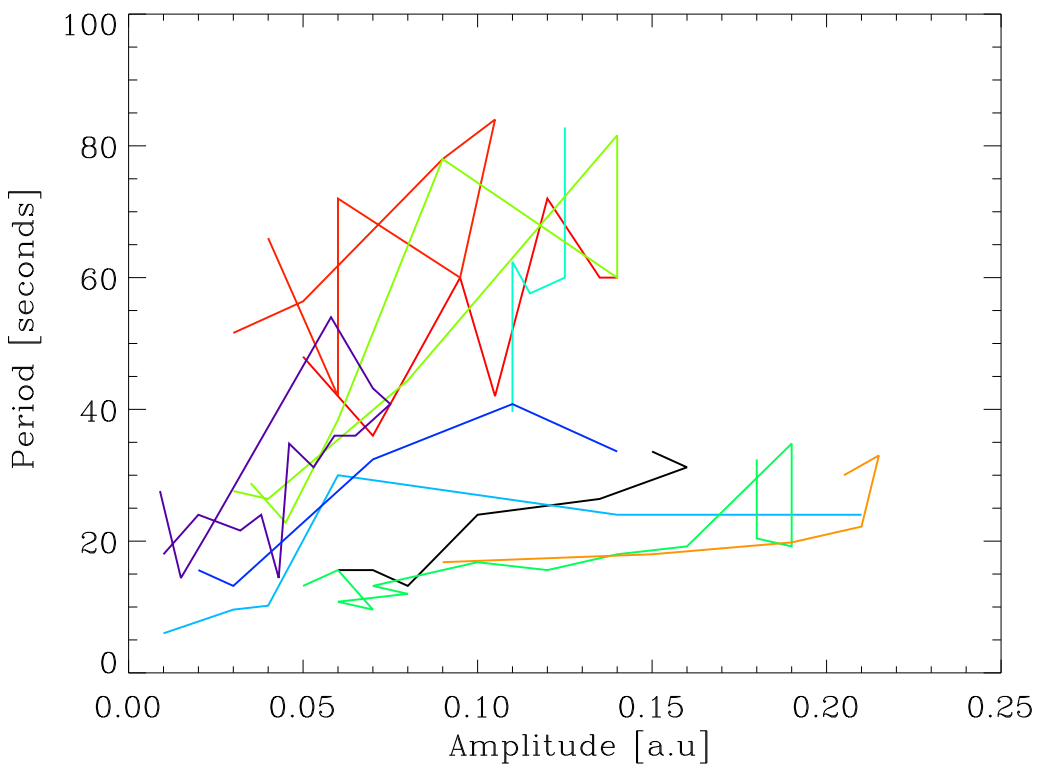


Figure 5.7: The proportionality between amplitude and instantaneous period for 11 events shown as different coloured lines, of which ten originated from the active region 12172/12192/12209, discussed in Chapter 5. A positive correlation can be seen between the instantaneous amplitudes and periods.

# Chapter 6

## Discussion and conclusion

### 6.1 Discussion of findings

#### 6.1.1 Remarks on the use of EMD in the context of solar data

As shown in this thesis, particularly in the Hare and Hounds exercise (Chapter 3) and the comparison of Methods 1 and 2 (Chapter 5), EMD presents an alternative method of analysing quasi-periodic signals and shows, in general, good agreements with well respected methods built on traditional Fourier analysis. This confirmation should encourage support for results obtained by EMD to be used in comparison to, and in support of, more widely used techniques in the solar community. As noted in Chapter 3, EMD is particularly useful when used to analyse non-stationary signals that do not exhibit harmonic behaviour. In these cases, both wavelet and Fourier analysis (and by extension any techniques derived from similar origins) cannot be applied as an output of a sinusoidal function is expected. As EMD does not enforce such expectations it is extremely well-suited to obtain non-stationary results. As demonstrated in Figure 3.1, the use of both wavelet and EMD seems to be an ideal compromise for analysing signals when the degree of non-stationarity is unknown. As wavelet analysis is well respected and computationally efficient, a simple spectrum could be produced for each trimmed lightcurve, around an area that shows oscillatory behaviour. Then, if the spectrum shows evidence of a period drift (as Figure 3.1 does), it would be sensible to allow the lightcurve to be analysed using the more time-intensive EMD technique which will produce a far more appropriate IMF that may appear anharmonic and may, for example, exhibit a correlation between QPP parameters such as period and amplitude (see Section 5.3). Similarly the initial analysis could be carried out by a Fourier transform and evidence of a peak in the Fourier power spectrum being spread over a significant range may suggest that

EMD analysis is better suited for the analysis of the possibly non-stationary signal.

It is encouraged for all EMD analysis to be carried out in tandem with a traditional method in any case, as due to the sensitivity of the shift factor (See Section 2.2), many modes of varying periodicities above a given confidence interval may be extracted, not all of which are appropriate choices for the light curve in question. By using the region(s) of period(s) deemed statistically significant by Fourier analysis, for example, the window of values for an appropriate choice of shift factor may be determined so that the outputted periods of the significant IMFs match with those determined with Fourier analysis. Furthermore, due to the time consuming nature of EMD it is more sensible to use faster, more efficient and less subjective methods when analysing curves that show stationary behaviour. However it should be noted that Fourier based methods also have a degree of subjectivity; in the choice of time intervals, zero-padding, choice of wavelet motherfunction and so on.

Other complications arise in signals which present evidence of multiple events separated in time. Much like other data analysis techniques, EMD requires a lightcurve to be separated into independent events and analysed separately. However, if multiple events occur simultaneously, the EMD code can be run repetitively, removing one significant mode each time, in effect reducing the curve into its overlayed IMFs. Thus EMD can be used to extract a highly significant low frequency oscillation which can be taken as the trend of the data and so EMD could be applied as a technique of detrending, as an alternative to smoothing or application of an  $n^{\text{th}}$ -order polynomial. Therefore EMD can be used to great effect and could be a helpful tool for solar physicists performing data analysis, when used in the appropriate circumstances.

### 6.1.2 Mechanisms needed for the classification of QPPs

Section 5.2 outlines an encouraging step towards classifying QPPs. Relationships between different properties, such as a dependence of frequency on amplitude, may be caused by the mechanisms generating the QPPs. Thus a large scale study of the QPP parameters could lead to grouping together oscillations into different subsets that could possibly be due to different regimes. The proportionality seen in Figure 5.7 could be evidence for a ‘magnetic dripping’ regime wherein the amplitude of the oscillation is modulated by its period. By finding the regimes driving QPPs, a better understanding of solar activity can be reached, and may qualify QPPs to be diagnostic tools for behaviour in active regions. This line of questioning can be followed by a larger scale study of parameters, possibly using other instruments to confirm any relationships for

better confidence in the results. Data from the Atmospheric Imaging Assembly (AIA) instrument aboard Solar Dynamics Observatory (SDO) could also be used to search for direct evidence of external drivers, such as a nearby oscillating loop near QPP sites.

### 6.1.3 Further work

Several projects could be pursued following the completion of the work outlined in this thesis. In particular it has been seen that EMD is a highly effective and valuable tool for examining non-stationary signals. However, due to the user requirements of manually inputting a shift factor, the analysis is relatively slow and cumbersome compared to Fourier and wavelet analysis. Therefore, any improvement in the efficiency of the EMD code would be extremely valuable and could be carried out by pre-selecting significant modes in a range found via wavelet analysis. This would remove the need for a user to pick an appropriate shift factor, and instead would run through many iterations of shift factors, selecting those that produce IMFs with periods corresponding to the range of periods found using wavelet analysis. Although this iterative technique would take some time to run, it could be allowed to run as a background program, allowing a user to only interact with the technique once an appropriate shift factor has been selected. This would improve the efficiency of the program in terms of the amount of time that a user has to actively interact with it.

The analysis performed in Chapter 4 seems to suggest a lack of periodic behaviour in the seven flaring events observed in HXR. However as all of these flares were only examined using RHESSI in the 50–100 keV channel, it would be sensible to revisit the events in the softer X-ray waveband, possibly using different instrumentation. This will allow for further confirmation that the behaviour is indeed aperiodic. In addition, the oscillation seen in Figure 4.2 should be examined in other energies and/or instruments in order to confirm its artificial origins. In terms of future work, additional candidates for an erupting magnetic flux tube could be analysed using EMD where a similar lack of periodicity would be expected. It is important to bear in mind that a theory for the production of irregular pulsations (as discussed in Chapter 4) by the unzipping/whipping mechanism has not yet been formulated and must be tested observationally. In addition it cannot be supported by this lack of periodicity alone. Similarly other means of production of these irregular pulsations must be considered, such as the reflection of the slow wave mechanism as developed by Nakariakov & Zimovets [2011].

In order to create a classification system for QPPs as a means to separate them into separate generation regimes, further work must be done to discern what distin-

guishes one class of QPPs from another. It may be wise to look initially for relationships that would be expected from a given generation mechanism, e.g. external drivers. This mechanism would suggest the period of oscillation to match closely with that of a neighbouring oscillatory system. This approach could then be applied to other methods such as MHD waves. Equally, a study looking at the relationships of many parameters blindly could be seen as a more honest and unbiased method of finding generation mechanisms for QPPs. It could uncover relationships which had not been previously considered and possibly bring candidates of new generation mechanisms to light, to allow the regime to fit the data, rather than seeking data to fit the hypothesis. Although the preliminary work put forward in Section 5.2 shows encouraging results for a magnetic dripping regime, this area must be looked at much closer across a larger dataset. Other candidates responsible for creating this apparent relationship between amplitude and instantaneous period should also be considered so as this phenomenon is not falsely attributed to the magnetic dripping regime when caused by another underlying behaviour.

# Bibliography

- Bahng, J., & Schwarzschild, M. 1961, *The Astrophysical Journal*, 134, 312
- Brodrick, D., Tingay, S., & Wieringa, M. 2005, *Journal of Geophysical Research: Space Physics*, 110
- Broomhall, A.-M., Hayes, L. A., Inglis, A. R., et al. 2018, (in prep)
- Carmichael, H. 1964, *NASA Special Publication*, 50, 451
- Craig, I. J. D., & McClymont, A. N. 1991, *The Astrophysical Journal Letters*, 371, L41
- Davenport, J. R. A., Hawley, S. L., Hebb, L., et al. 2014, *The Astrophysical Journal*, 797, 122
- Dennis, B. R., Tolbert, A. K., Inglis, A., et al. 2017, *The Astrophysical Journal*, 836, 84
- Dolla, L., Marqué, C., Seaton, D. B., et al. 2012, *The Astrophysical Journal Letters*, 749, L16
- Doorsselaere, T. V., Groof, A. D., Zender, J., Berghmans, D., & Goossens, M. 2011, *The Astrophysical Journal*, 740, 90
- Duckenfield, T., Anfinogentov, S. A., Pascoe, D. J., & Nakariakov, V. M. 2018, *The Astrophysical Journal Letters*, 854, L5
- Gallagher, P. T., Moon, Y.-J., & Wang, H. 2002, *Solar Physics*, 209, 171
- Hirayama, T. 1974, *Solar Physics*, 34, 323
- Huang, N. E., & Wu, Z. 2008, *Reviews of Geophysics*, 46
- Huang, N. E., Shen, Z., Long, S. R., et al. 1998, *Proceedings of the Royal Society of London A: Mathematical, Physical and Engineering Sciences*, 454, 903

- Hurford, G., Schmahl, E., Schwartz, R., et al. 2002, *Solar Physics*, 210, 61
- Inglis, A. R., Ireland, J., Dennis, B. R., Hayes, L., & Gallagher, P. 2016, *The Astrophysical Journal*, 833, 284
- Inglis, A. R., Ireland, J., & Dominique, M. 2015, *The Astrophysical Journal*, 798, 108
- Inglis, A. R., Nakariakov, V. M., & Melnikov, V. F. 2008, *Astronomy & Astrophysics*, 487, 1147
- Inglis, A. R., Zimovets, I. V., Dennis, B. R., et al. 2011, *Astronomy & Astrophysics*, 530, A47
- Kolotkov, D. Y., Anfinogentov, S. A., & Nakariakov, V. M. 2016, *Astronomy & Astrophysics*, 592, A153
- Kolotkov, D. Y., Nakariakov, V. M., Kupriyanova, E. G., Ratcliffe, H., & Shibasaki, K. 2015, *Astronomy & Astrophysics*, 574, A53
- Kopp, R. A., & Pneuman, G. W. 1976, *Solar Physics*, 50, 85
- Kuznetsov, S. A., Zimovets, I. V., Morgachev, A. S., & Sturinsky, A. B. 2016, *Solar Physics*, 291, 3385
- Leighton, R. B., Noyes, R. W., & Simon, G. W. 1962, *The Astrophysical Journal*, 135, 474
- Liu, R., Alexandar, D., & Gilbert, H. 2009, *The Astrophysical Journal*, 691, 1079
- Loh, C.-H., Wu, T.-C., & Huang, N. E. 2001, *Bulletin of the Seismological Society of America*, 91, 1339
- Machol, J., & Viereck, R. 2016, GOES X-ray Sensor (XRS) Measurements, 1–14
- McCloskey, A. E., Gallagher, P. T., & Bloomfield, D. S. 2016, *Solar Physics*, 291, 1711
- McLaughlin, J. A., Nakariakov, V. M., Dominique, M., Jelínek, P., & Takasao, S. 2018, *Space Science Reviews*, 214, 45
- Meegan, C., Lichti, G., Bhat, P. N., et al. 2009, *The Astrophysical Journal*, 702, 791
- Myagkova, I. N., Bogomolov, A. V., Kashapova, L. K., et al. 2016, *Solar Physics*, 291, 3439

- N. Bracewell, R. 1989, The Fourier Transform, Vol. 260, 86–95
- Nakajima, H., Nishio, M., Enome, S., et al. 1994, IEEE Proceedings, 82, 705
- Nakariakov, V. M., Foulon, C., Verwichte, E., & Young, N. P. 2006, *Astronomy & Astrophysics*, 452, 343
- Nakariakov, V. M., Inglis, A. R., Zimovets, I. V., et al. 2010, *Plasma Physics and Controlled Fusion*, 52, 124009
- Nakariakov, V. M., Kolotkov, D. Y., Kupriyanova, E. G., et al. 2018, (in press)
- Nakariakov, V. M., & Melnikov, V. F. 2009, *Space Science Review*, 149, 119
- Nakariakov, V. M., & Zimovets, I. V. 2011, *The Astrophysical Journal Letters*, 730, L27
- Parks, G. K., & Winckler, J. R. 1969, *The Astrophysical Journal*, 155, L117
- Phillips, T. 2008, What's wrong with the Sun?
- Pugh, C. E., Armstrong, D. J., Nakariakov, V. M., & Broomhall, A.-M. 2016, *Monthly Notices of the Royal Astronomical Society*, 459, 3659
- Pugh, C. E., Broomhall, A.-M., & Nakariakov, V. M. 2017a, *Astronomy & Astrophysics*, 602, A47
- Pugh, C. E., Nakariakov, V. M., Broomhall, A.-M., Bogomolov, A. V., & Myagkova, I. N. 2017b, *Astronomy & Astrophysics*, 608, A101
- Sturrock, P. A. 1966, *Nature*, 211, 695
- Torrence, C., & Compo, G. P. 1998, *Bulletin of the American Meteorological Society*, 79, 61
- Van Doorsselaere, T., Kupriyanova, E. G., & Yuan, D. 2016, *Solar Physics*, 291, 3143
- Vaughan, S. 2005, *Astronomy & Astrophysics*, 431, 391
- Veronig, A. M., Brown, J. C., Dennis, B. R., et al. 2005, *The Astrophysical Journal*, 621, 482
- Zimovets, I. V., Wang, R., Liu, Y. D., et al. 2018, *Journal of Atmospheric and Solar-Terrestrial Physics*, 174, 17

## Appendix A

# Comparison of results from Chapter 5

This appendix presents full tables of results from the analysis carried out in Section 5.1, from Nobeyama RadioHeliograph, *Vernov*, *Fermi*, and GOES. The ‘Flare number’ is as defined in Pugh et al. [2017b].  $P_{M.1}$  refers to the period in seconds obtained by Method 1 as outlined in Pugh et al. [2017b], similarly for  $P_{M.2}$  which refers to the EMD method discussed in this thesis, outlined in Section 2.2. Agreement is denoted with ‘Y’ if the periods lie within 5.0 s of one another, and ‘N’ if not. ‘/’ is given if no significant period was obtained during analysis by Method 2. The time intervals were kept roughly the same from the intervals given in Pugh et al. [2017b], but were modified by up to 10 s to allow more appropriate intrinsic mode functions to be selected. The channels with which the oscillations were recorded were maintained from Pugh et al. [2017b], excluding the 030 GOES event in which Method 1 made an initial detection in the 0.5–4 Å channel, but a significant oscillation was observed in the 1–8 Å channel by Method 2.

Table A.1: Summary table of comparative results from Nobeyama RadioHeliograph

Flare No.	Start Time	End Time	$P_{M.1}$ (s)	$P_{M.2}$ (s)	Agreement
022	2014-10-17 05:23:18	2014-10-17 05:26:35	39.2	/	/
027	2014-10-18 01:04:10	2014-10-18 01:08:30	8.0	137.6	N
037	2014-10-19 01:36:28	2014-10-19 01:42:42	24.9	25.8	Y
079	2014-10-24 02:38:30	2014-10-24 02:41:20	7.9	/	/
081	2014-10-24 03:59:30	2014-10-24 04:01:00	14.8	16.9	Y
138	2014-10-29 23:44:16	2014-10-29 23:45:48	10.1	/	/
142	2014-10-30 05:44:27	2014-10-30 05:45:43	18.7	16.9	Y
147	2014-11-13 06:04:59	2014-11-13 06:07:15	9.0	29.5	N

Table A.2: Summary table of comparative results from *Vernov*

Flare No.	Start Time	End Time	$P_{M.1}$ (s)	$P_{M.2}$ (s)	Agreement
010	2014-09-24 17:49:01	2014-09-24 17:49:50	5.8	8.9	Y
056	2014-10-20 18:57:53	2014-10-20 18:59:02	17.2	11.1	N
135	2014-10-29 21:21:28	2014-10-29 21:22:52	7.6	/	/

Table A.3: Summary table of comparative results from *Fermi*

Flare No.	Start Time	End Time	Channel (keV)	$P_{M.1}$ (s)	$P_{M.2}$ (s)	Agreement
056	2014-10-20 18:57:51	2014-10-20 18:59:01	25–50	13.9	/	/
072	2014-10-22 14:06:55	2014-10-22 14:12:02	50–100	30.6	32.5	Y
098	2014-10-26 10:48:52	2014-10-26 10:50:34	25–50	20.3	44.6	N
104	2014-10-26 18:12:40	2014-10-26 18:15:28	25–50	20.9	21.0	Y
106	2014-10-26 20:03:38	2014-10-26 20:09:02	25–50	31.9	61.3	N
135	2014-10-29 21:21:33	2014-10-29 21:22:19	25–50	7.5	29.3	N

Table A.4: Summary table of comparative results from GOES

Flare No.	Start Time	End Time	Channel (Å)	P <sub>M.1</sub> (s)	P <sub>M.2</sub> (s)	Agreement
008	2014-09-23 23:08:20	2014-09-23 23:13:52	0.5–4	41.2	43.0	Y
010	2014-09-24 17:49:04	2014-09-24 17:50:18	1–8	9.6	9.7	Y
024	2014-10-17 15:35:30	2014-10-17 15:37:54	1–8	22.1	23.3	Y
029	2014-10-18 07:36:14	2014-10-18 07:48:48	1–8	50.1	55.5	N
030	2014-10-18 13:14:38	2014-10-18 13:15:52	0.5–4*	14.3	14.8	Y
035	2014-10-18 19:02:30	2014-10-18 19:06:58	1–8	13.3	/	/
037	2014-10-19 01:35:00	2014-10-19 01:43:00	0.5–4	79.5	78.7	Y
038	2014-10-19 04:20:24	2014-10-19 04:24:56	1–8	53.7	59.5	N
038	2014-10-19 04:20:24	2014-10-19 04:24:56	0.5–4	24.4	54.3	N
038	2014-10-19 04:41:39	2014-10-19 04:50:00	0.5–4	45.4	44.9	Y
049	2014-10-20 09:05:45	2014-10-20 09:08:14	0.5–4	14.7	14.1	Y
052	2014-10-20 14:41:47	2014-10-20 14:43:33	1–8	26.1	27.6	Y
054	2014-10-20 16:23:02	2014-10-20 16:31:20	1–8	35.4	135.8	N
058	2014-10-20 22:45:18	2014-10-20 22:49:46	1–8	48.4	47.7	Y
058	2014-10-20 22:45:18	2014-10-20 22:49:46	0.5–4	48.4	47.7	Y
068	2014-10-22 01:43:04	2014-10-22 01:46:36	1–8	21.1	79.1	N
068	2014-10-22 01:43:04	2014-10-22 01:46:36	0.5–4	21.1	/	/
072	2014-10-22 14:06:56	2014-10-22 14:09:30	1–8	30.3	27.5	Y
072	2014-10-22 14:15:24	2014-10-22 14:23:40	0.5–4	49.4	46.9	Y
085	2014-10-24 21:19:38	2014-10-24 21:23:47	0.5–4	49.6	52.6	Y
092	2014-10-25 17:02:11	2014-10-25 17:10:10	1–8	25.1	23.2	Y
092	2014-10-25 17:02:11	2014-10-25 17:10:10	0.5–4	25.1	24.3	Y
104	2014-10-26 18:11:18	2014-10-26 18:15:24	0.5–4	20.3	21.2	Y
105	2014-10-26 18:45:04	2014-10-26 18:48:02	1–8	25.2	24.5	Y
106	2014-10-26 20:03:42	2014-10-26 20:11:18	1–8	36.4	33.9	Y
106	2014-10-26 20:03:42	2014-10-26 20:11:18	0.5–4	36.4	34.6	Y
117	2014-10-27 17:36:36	2014-10-27 17:37:26	1–8	12.3	10.6	Y
140	2014-10-30 01:28:38	2014-10-30 01:30:30	1–8	24.6	30.2	N
141	2014-10-30 04:22:08	2014-10-30 04:28:00	1–8	21.9	/	/
142	2014-10-30 05:44:27	2014-10-30 05:45:45	1–8	18.9	17.4	Y
152	2014-11-15 11:56:08	2014-11-15 12:02:58	1–8	27.2	27.2	Y
152	2014-11-15 11:56:08	2014-11-15 12:02:58	0.5–4	27.2	27.4	Y
153	2014-11-15 20:42:57	2014-11-15 20:44:28	0.5–4	20.0	/	/
161	2014-11-16 17:42:46	2014-11-16 17:45:24	0.5–4	19.5	18.6	Y
177	2014-11-22 06:02:16	2014-11-22 06:04:48	1–8	18.7	20.4	Y
177	2014-11-22 06:02:16	2014-11-22 06:04:48	0.5–4	18.7	18.0	Y

\*This event was observed in the 0.5–4 Å channel by Method 1 and 1–8 Å channel by Method 2